ARTICLES
https://doi.org/10.1038/s43587-021-00073-z

nature aging

APOE4 accelerates advanced-stage vascular and neurodegenerative disorder in old Alzheimer's mice via cyclophilin A independently of amyloid-β

Axel Montagne[1,4], Angeliki M. Nikolakopoulou[1,4], Mikko T. Huuskonen[1,4], Abhay P. Sagare[1,4], Erica J. Lawson[1], Divna Lazic[1], Sanket V. Rege[1], Alexandra Grond[1], Edward Zuniga[1], Samuel R. Barnes[2], Jacob Prince[1], Meghana Sagare[1], Ching-Ju Hsu[1], Mary J. LaDu[3], Russell E. Jacobs[1] and Berislav V. Zlokovic[1]✉

Apolipoprotein E4 (*APOE4*), the main susceptibility gene for Alzheimer's disease (AD), leads to vascular dysfunction, amyloid-β pathology, neurodegeneration and dementia. How these different pathologies contribute to advanced-stage AD remains unclear. Using aged APOE knock-in mice crossed with *5xFAD* mice, we show that, compared to APOE3, APOE4 accelerates blood–brain barrier (BBB) breakdown, loss of cerebral blood flow, neuronal loss and behavioral deficits independently of amyloid-β. BBB breakdown was associated with activation of the cyclophilin A-matrix metalloproteinase-9 BBB-degrading pathway in pericytes. Suppression of this pathway improved BBB integrity and prevented further neuronal loss and behavioral deficits in APOE4;5FAD mice while having no effect on amyloid-β pathology. Thus, APOE4 accelerates advanced-stage BBB breakdown and neurodegeneration in Alzheimer's mice via the cyclophilin A pathway in pericytes independently of amyloid-β, which has implication for the pathogenesis and treatment of vascular and neurodegenerative disorder in AD.

The *APOE4* variant of apolipoprotein E is the strongest genetic risk factor for AD[1]. One and two *APOE4* alleles increase risk for AD by approximately 4- and 15-fold, respectively, compared to the more-common *APOE3* gene that carries lower risk for AD[1]. Besides accelerating onset and progression of dementia, *APOE4* is associated with different brain pathologies. For example, *APOE4* accelerates BBB breakdown and degeneration of brain capillary pericytes[2,3] that maintain BBB integrity[4–6] and leads to cerebral blood flow (CBF) reduction[7,8] and dysregulation[7,9,10]. *APOE4* is toxic to neurons[11] and accelerates tau-mediated neurodegeneration[12]. Additionally, *APOE4* slows down amyloid-β (Aβ) clearance[13,14] and accelerates amyloid deposition[14–16], which promotes development of amyloid pathology.

Recent studies focused on very early stages in the Alzheimer's continuum in individuals who are cognitively unimpaired or with mild cognitive impairment (MCI) have shown that individuals bearing an *APOE4* variant (*APOE3*/*APOE4* or *APOE4*/*APOE4*) are distinguished from *APOE3* homozygotes by breakdown in the BBB in the hippocampus and medial temporal lobe, regions responsible for memory encoding and cognitive functions[17]. This finding is apparent in cognitively unimpaired *APOE4* carriers and more severe in those with MCI and is independent of Aβ or tau pathology measured in the cerebrospinal fluid or in brain by positron emission tomography[17]. These findings support the growing evidence suggesting that vascular dysfunction, BBB breakdown and vascular disorder contribute to early cognitive impairment and AD[17–26]. On the other hand, accumulation of Aβ in the brain has also been suggested to occur years before cognitive impairment and continues to increase with disease progression[27]. Although it has been shown that vascular dysfunction contributes to early cognitive impairment in ways that may not be exclusively related to classical AD pathology[17,19,20,26], the respective contributions of the BBB pathway and vascular disorder versus amyloid-β pathway to advanced disease stage during progression of neurodegenerative disorder and cognitive decline in AD are still poorly understood.

To address this question, here we studied vascular dysfunction, Aβ pathology, neuronal dysfunction and behavior in older *APOE3* and *APOE4* knock-in mice[28] alone and crossed with the *5xFAD* line[29]. All mice were derived from the same litters, as previously described[30]. Mice lacking *Apoe*[3] and/or expressing human *APOE4* develop early BBB breakdown[3,31–33] and CBF dysregulation[10]. On the other hand, the *5xFAD* line also develops BBB breakdown[34–37], CBF reductions[38] and neuron and synaptic loss at a later stage[29,39], whereas *APOE3;5xFAD* and *APOE4;5xFAD* mice (also known as *E3FAD* and *E4FAD* lines, respectively[30]) have comparable Aβ pathology at an older age[40]. These features of the studied models allowed us to interrogate how different pathologies in *APOE4* compared to *APOE3* mice relate to each other and how they influence neuronal function and behavior.

Results

Blood–brain barrier breakdown in *APOE4* and *APOE4;5xFAD* mice. First, we studied BBB integrity in the cortex and hippocampus in 18–24-month-old *APOE3* and *APOE4* knock-in controls and *APOE3;5xFAD* and *APOE4;5xFAD* mice derived from the same litters, as previously described[30]. Using a dynamic contrast-enhanced

[1]Department of Physiology and Neuroscience, Zilkha Neurogenetic Institute, Keck School of Medicine, University of Southern California, Los Angeles, CA, USA. [2]Department of Radiology, Loma Linda University, Loma Linda, CA, USA. [3]Department of Anatomy and Cell Biology, College of Medicine, University of Illinois at Chicago, Chicago, IL, USA. [4]These authors contributed equally: Axel Montagne, Angeliki M. Nikolakopoulou, Mikko T. Huuskonen, Abhay P. Sagare. ✉e-mail: zlokovic@usc.edu

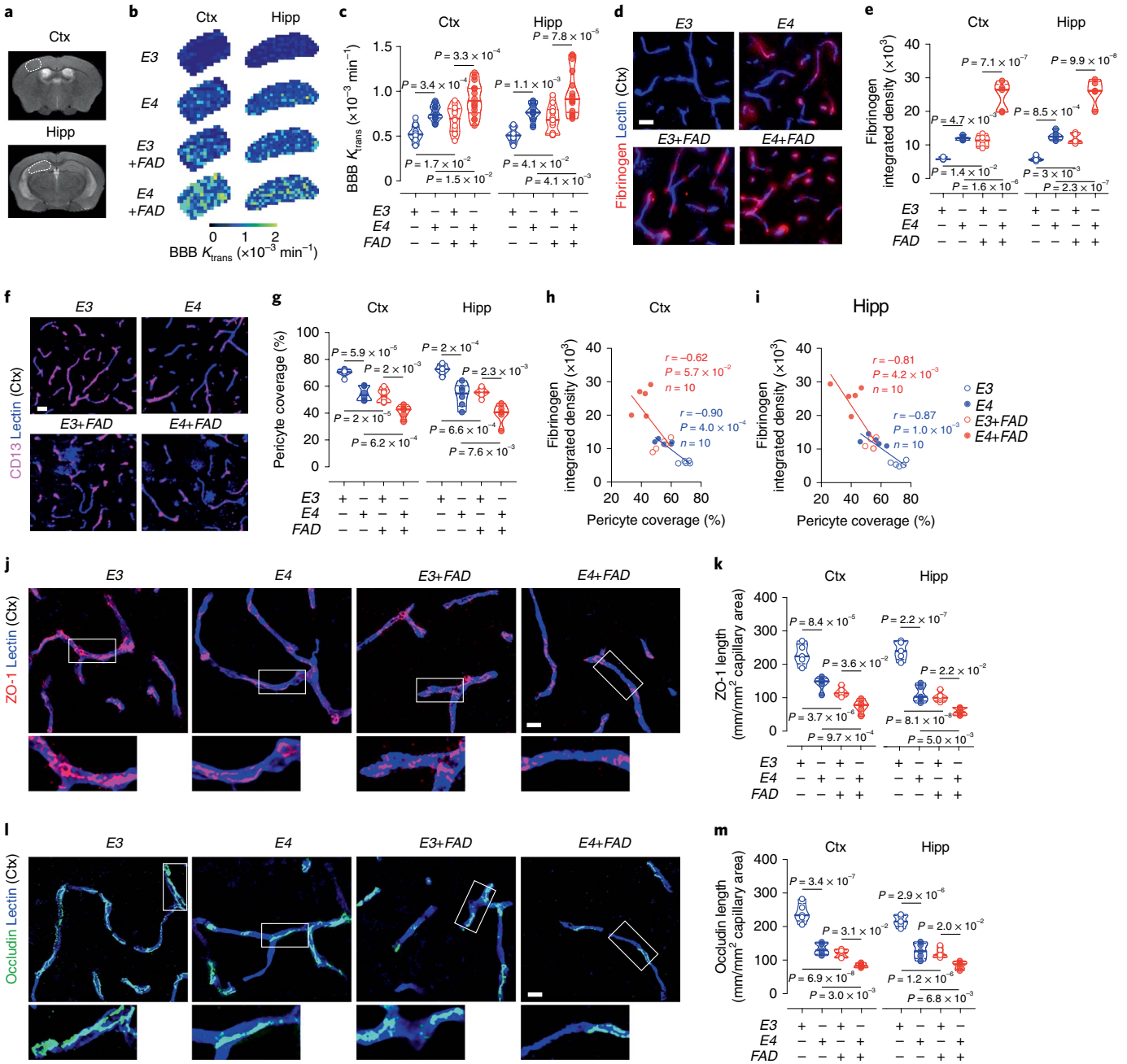

Fig. 1 | Blood–brain barrier breakdown in old *APOE4* and *APOE4;5xFAD* mice. a, T2-weighted scans displaying regions of interest: primary somatosensory cortex (Ctx) and hippocampus (Hipp). **b**,**c**, Representative K_{trans} maps (**b**) and BBB permeability K_{trans} values (**c**) in the Ctx and Hipp in *APOE3* (*E3*, $n=12$; blue empty circles), *APOE4* (*E4*, $n=14$; blue-filled circles), *APOE3;5xFAD* (*E3+FAD*, $n=13$; red empty circles) and *APOE4;5xFAD* (*E4+FAD*, $n=16$; red-filled circles) mice generated from DCE-MRI scans. **d**,**e**, Fibrinogen$^+$ perivascular capillary deposits (red) in the Ctx (**d**) and quantification of fibrinogen$^+$ deposits in the Ctx and Hipp (**e**) in *E3*, *E4*, *E3+FAD* and *E4+FAD* mice. Blue, lectin$^+$ endothelial profiles; $n=5$ mice per group; scale bar, 20 µm. **f**,**g**, CD13$^+$ pericyte coverage (magenta) of lectin$^+$ endothelial capillary profiles (blue) in the Ctx (**f**) and quantification of pericyte coverage on capillaries in the Ctx and Hipp (**g**) in *E3* ($n=6$), *E4* ($n=6$), *E3+FAD* ($n=6$) and *E4+FAD* ($n=5$) mice; scale bar, 20 µm. **h**,**i**, Negative correlation between fibrinogen deposits and pericyte coverage in the Ctx (**h**) and Hipp (**i**) using individual mouse data points from the studied groups. Mice (both sexes) were 18–24 months old. **j**–**m**, Representative immunostaining for ZO-1 (red) and lectin$^+$ endothelium (blue) in the Ctx (**l**, red) and ZO-1 length in the Ctx and Hipp (**k**) and immunostaining for occludin (green) and lectin$^+$ endothelium (blue) in the Ctx (**l**, green) and occludin length in the Ctx and Hipp (**m**) in *E3* (blue empty circles), *E4* (blue-filled circles), *E3+FAD* (red empty circles) and *E4+FAD* (red-filled circles) mice; $n=5$ mice/group; scale bar, 20 µm. Boxes in **j** and **l** denote sites taken for higher magnification insets shown below merged images. Mice (both sexes) were 18–24 months old. In **c**,**e**,**g**,**k** and **m** data are presented as truncated violin plots; continuous line, median; and dotted line, interquartile range. Significance by one-way analysis of variance (ANOVA) followed by the Tukey post hoc test. Significance by two-tailed simple linear regression (**h**,**i**); *r*, Pearson correlation coefficient.

magnetic resonance imaging (DCE-MRI) protocol as we previously developed[6,41], we found that *APOE4* mice compared to the respective *APOE3* lines develop accelerated BBB breakdown in the cortex and hippocampus both without and with Aβ pathology (Fig. 1a–c), as shown by 43% and 52% and 29% and 34% increases in the BBB permeability K_{trans} values in *APOE4* versus *APOE3* mice alone and

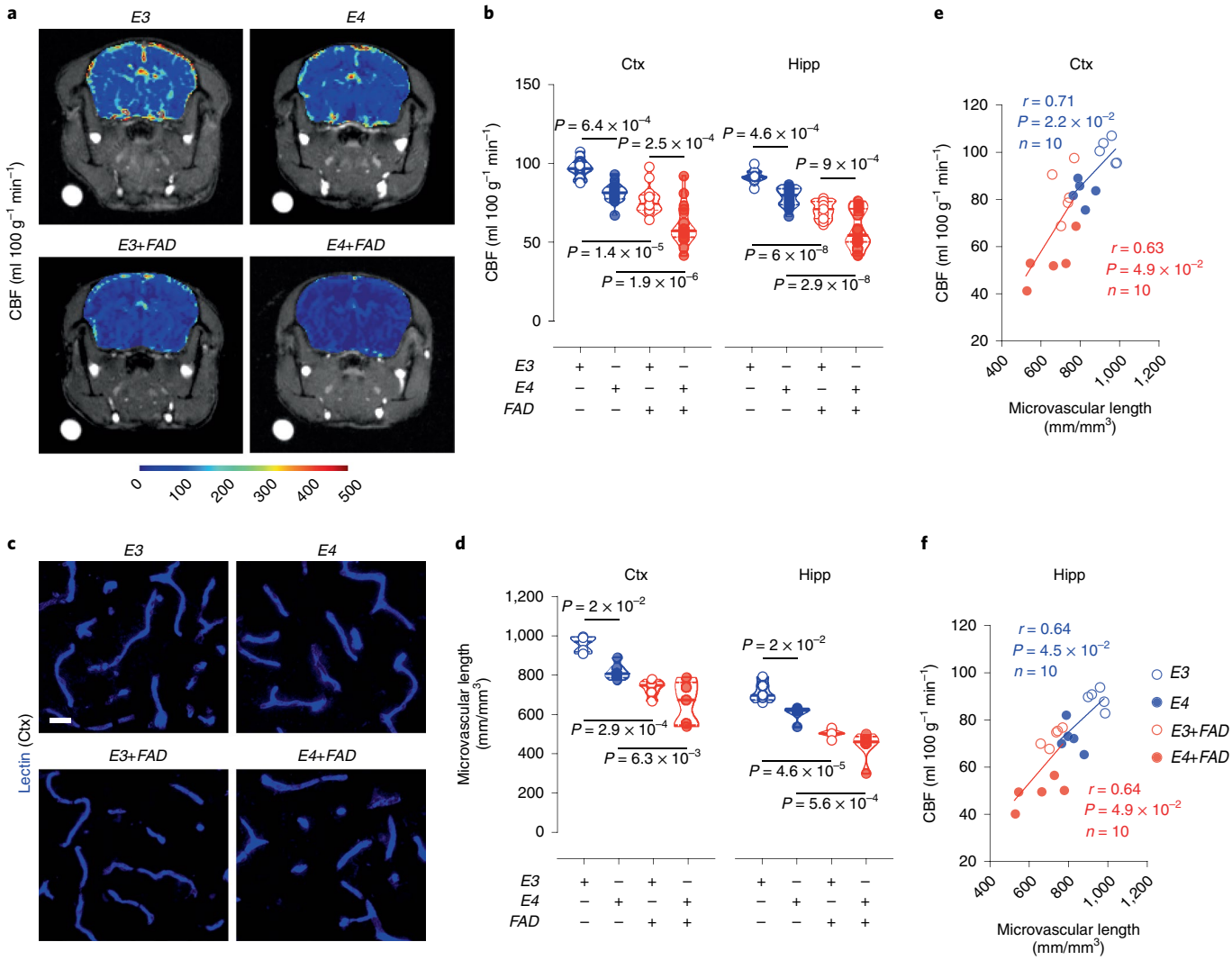

Fig. 2 | Cerebral blood flow reductions in old *APOE4* and *APOE4;5xFAD* mice. a,**b**, Representative CBF maps (**a**) and regional CBF values (**b**) in the cortex (Ctx) and hippocampus (Hipp) in *E3* ($n=12$; blue empty circles), *E4* ($n=14$; blue-filled circles), *E3+FAD* ($n=13$; red empty circles) and *E4+FAD* ($n=16$; red-filled circles) mice generated from dynamic susceptibility-contrast magnetic resonance scans. **c**,**d**, Representative lectin$^+$ endothelial profiles (blue) in the Ctx (**c**) and microvascular length in the Ctx and Hipp (**d**) in *E3*, *E4*, *E3+FAD* and *E4+FAD* mice; $n=5$ mice/group; scale bar, 20 µm. **e**,**f**, Positive correlation between the CBF and microvascular length in the Ctx (**e**) and Hipp (**f**) using individual mouse data points from the studied groups. Mice (both sexes) were 18–24 months old. In **b** and **d**, data are presented as truncated violin plots; continuous line, median; and dotted line, interquartile range. Significance by one-way ANOVA followed by the Tukey post hoc test. In **e** and **f**, significance was determined by two-tailed simple linear regression.

in these mice crossed with *5xFAD* mice, respectively (Fig. 1b,c). We also found substantial 35% and 36% and 22% and 20% increases in regional BBB K_{trans} values in the cortex and hippocampus of *APOE3;5xFAD* and *APOE4;5xFAD* mice compared to their respective *APOE3* and *APOE4* littermate controls (Fig. 1c), consistent with previously shown BBB breakdown in *5xFAD* mice[34–37].

These results were confirmed by increased levels of perivascular brain capillary cortical and hippocampal deposits of blood-derived fibrinogen in *APOE4* compared to *APOE3* mice both in the presence and absence of Aβ pathology (Fig. 1d,e). Specifically, we found 111% and 122% and 135% and 137% increase in fibrinogen deposits in the cortex and hippocampus in *APOE4* versus *APOE3* mice alone and in these mice crossed with *5xFAD* mice, respectively (Fig. 1e). The effects of Aβ pathology was evident in both genotypes when compared to knock-in littermate controls (Fig. 1d,e), consistent with previously reported BBB breakdown in *5xFAD* mice.

In contrast to a previous study showing that younger 8-month-old *APOE4;5xFAD* female mice had higher BBB leakiness compared to male mice[42], the present study did not find the effect of gender on the regional BBB K_{trans} values in either *APOE4* versus *APOE3* mice alone and/or in these mice crossed with *5xFAD* mice (Extended Data Fig. 1). Whether the difference between previous studies[42] and the current study reflects a difference in age (18–24 versus 8 months old) and/or whether female mice develop less severe BBB impairment with age or alternatively, males develop more rapid BBB changes with age, remains an interesting topic for future studies.

Compared to *APOE3* mice, *APOE4* littermate controls showed loss of brain capillary pericyte coverage in the cortex and hippocampus (Fig. 1f,g). For example, *APOE4* compared to *APOE3* mice alone and crossed with *5xFAD* mice had 24% and 25% and 19% and 27% loss of pericyte coverage in the cortex and hippocampus, respectively (Fig. 1g). These findings were consistent with previously shown loss of pericyte coverage in *APOE4* mice[3]. The effect of Aβ pathology on loss of pericyte coverage was seen in both genotypes, again consistent with findings showing loss of pericytes in AD mouse lines[43–45]. However, the effect was much more

pronounced in *APOE4* than in *APOE3* mice. The regional accumulation of perivascular brain capillary fibrinogen deposits negatively correlated with loss of pericyte coverage (Fig. 1h,i), similar to that reported in pericyte-deficient mouse lines[5,41].

The analysis of the BBB tight junction proteins revealed loss in the zonula occludens-1 (ZO-1) and occludin length coverage in *APOE4* compared to *APOE3* mice both in the presence and absence of Aβ pathology (Fig. 1l,m). We found substantial 34% and 57% and 31% and 42% loss in ZO-1 length and 45% and 42% and 31% and 25% loss in occludin length in the cortex and hippocampus of *APOE3* and *APOE4* littermate controls alone and in these mice crossed with *5xFAD* mice, respectively (Fig. 1k,m). These findings were consistent with previously shown losses of the BBB tight junction proteins in *APOE4* (ref. [3]) and *5xFAD*[34] mice.

Cerebral blood flow reductions in *APOE4* and *APOE4;5xFAD* mice. Next, we studied CBF changes in the cortex and hippocampus in 18–24-month-old *APOE3* and *APOE4* knock-in littermate controls and *APOE3;5xFAD* and *APOE4;5xFAD* mice, using a dynamic susceptibility-contrast (DSC)-MRI protocol as we previously developed[6,41]. We found that *APOE4* compared to *APOE3* mice develop a moderate, but substantial CBF loss in the cortex and hippocampus both in the presence and absence of Aβ pathology (Fig. 2a,b). This has been shown by 16% and 13% and 24% and 24% reductions in the regional cortical and hippocampal CBF in *APOE4* vs. *APOE3* mice alone and in these mice crossed with *5xFAD* mice, respectively (Fig. 2a,b). Additionally, we found substantial 23% and 23% and 31% and 33% reductions in the cortical and hippocampal CBF in *5xFAD* mice crossed to *APOE3* and *APOE4* mice compared to their respective knock-in littermate controls (Fig. 2b). As with BBB breakdown, sex did not have an effect on regional CBF changes in old mice (Extended Data Fig. 2).

Compared to *APOE3* mice, *APOE4* mice had also a moderate but substantial loss of capillary density in the cortex and hippocampus both in the presence and absence of Aβ pathology (Fig. 2c,d), as shown by 17% and 11% and 10% and 9% reductions in the cortical and hippocampal capillary length in *APOE4* versus *APOE3* littermate control mice and *APOE4;5xFAD* versus *APOE3;5xFAD* mice, respectively (Fig. 2d). CBF reductions positively correlated with reductions in the capillary length (Fig. 2e,f). The observed correlations were consistent with previously reported correlations between reductions in the CBF and microvascular density in pericyte-deficient[5,6,41] and *APOE4* (refs. [3,10]) mice.

Cyclophilin A-matrix metalloproteinase-9 pathway. In a search of a mechanism underlying vascular changes in *APOE4* compared to the respective *APOE3* lines, we focused on the BBB-degrading pro-inflammatory cyclophilin A (CypA)-matrix metalloproteinase (MMP)-9 pathway. When activated by brain capillary pericytes in *APOE4* but not *APOE3* transgenic mice, this pathway leads to MMP9-mediated breakdown of the BBB via degradation of BBB tight junction proteins, which in turn leads to leakages of blood-derived toxic proteins causing neuronal stress and dysfunction[3]. Previous work using in vivo multiphoton microscopy of DQ-gelatin has shown increased gelatinase MMP cerebrovascular activity in *APOE4* compared to *APOE3* mice, which has been confirmed by gelatin zymography of brain tissue, demonstrating an increase in pro-MMP9 and activated MMP9, but not MMP2 (ref. [3]).This pathway is also activated in human *APOE4* carriers diagnosed with AD, as suggested by neuropathological analysis[2] and in living human *APOE4* carriers, as shown by increased cerebrospinal fluid levels of CypA, MMP9 and sPDGFR-β, a marker of pericyte injury[17].

Immunocytochemical analysis indicated that *APOE4* mice compared to respective *APOE3* lines have higher levels of CypA$^+$ immunofluorescent signal in CD13$^+$ pericytes in the cortex and hippocampus both in the presence and absence of Aβ pathology (Fig. 3a,b). Specifically, we found 614% and 627% and 45% and 37% increases in CypA$^+$ signal in the cortical and hippocampal pericytes in *APOE4* compared to *APOE3* control mice alone and in these mice crossed with *5xFAD* mice, respectively (Fig. 3b). Increases in the CypA$^+$ immunofluorescent signal in CD13$^+$ pericytes in the cortex and hippocampus in *APOE4* compared to *APOE3* mice without *5xFAD* transgenes (littermate controls) and with *5xFAD* transgenes both negatively correlated with the reduced length of the tight junction proteins ZO-1 (Fig. 3c,d) and occludin (Fig. 3e,f), but the effect was more pronounced in mice expressing *5xFAD* transgenes, as expected based on the signal intensity data.

We also found increased MMP9$^+$ immunofluorescence signal in CD13$^+$-pericytes (Fig. 3g,h) by 406% and 412% and 47% and 61% in the cortex and hippocampus in *APOE4* compared to *APOE3* control mice alone and in these mice crossed with *5xFAD* mice, respectively (Fig. 3h). Increases in the MMP9$^+$ immunofluorescent signal in CD13$^+$ pericytes in the cortex and hippocampus also negatively correlated with the reduced length of ZO-1 (Fig. 3i,j) and occludin (Fig. 3k,l), as determined by immunostaining on adjacent sections. As expected, there was a positive correlation between the CypA$^+$ and MMP9$^+$ immunofluorescent signals in CD13$^+$ pericytes, both in the cortex and hippocampus, as shown by the correlation analysis using individual data points from both *APOE4* compared to *APOE3* mice without (littermate controls) and with *5xFAD* transgenes (Fig. 5m,n).

Altogether, these data demonstrate activation of the CypA-MMP9 pathway in pericytes in old *APOE4* and *APOE4;5xFAD* mice compared to the respective *APOE3* lines suggesting a possible mechanism for the *APOE4*-mediated BBB breakdown and loss of capillary density.

Aβ pathology and vascular dysfunction. As previously reported[40], we also found that levels of Aβ42, the principal Aβ peptide in

Fig. 3 | Increased levels of cyclophilin A and matrix metalloproteinase-9 in pericytes in old *APOE4* and *APOE4;5xFAD* mice correlate with the loss of tight junction proteins. a, Representative high-magnification confocal images of CD13$^+$ pericytes (green), cyclophilin A (CypA; red) and lectin$^+$ endothelium (blue) in the cortical capillaries in situ in *E3*, *E4*, *E3+FAD* and *E4+FAD* mice. Orthogonal views show colocalization of CypA with CD13$^+$ pericytes; scale bar, 10 µm. **b**, Quantification of CypA$^+$ pericytes in the cortex (Ctx) and hippocampus (Hipp) in *E3* (blue empty circles), *E4* (blue-filled circles), *E3+FAD* (red empty circles) and *E4+FAD* (red-filled circles) mice; $n=5$ mice/group. **c**–**f**, Negative correlation between CypA$^+$ pericytes and ZO-1 length (**c**,**d**), and CypA$^+$ pericytes and occludin length (**e**,**f**) in the Ctx and Hipp. **g**, Representative high-magnification confocal images of CD13$^+$ pericytes (green), MMP9 (red) and lectin$^+$ endothelium (blue) in the cortical capillaries in situ in *E3*, *E4*, *E3+FAD* and *E4+FAD* mice. Orthogonal views show colocalization of MMP9 with CD13$^+$ pericytes; scale bar, 10 µm. **h**, Quantification of MMP9$^+$ pericytes in the Ctx and Hipp in *E3* (blue empty circles), *E4* (blue-filled circles), *E3+FAD* (red empty circles) and *E4+FAD* (red empty circles) mice; $n=5$ mice/group. **i**–**l**, Negative correlation between MMP9$^+$ pericytes and ZO-1 length (**i**,**j**) and MMP9$^+$ pericytes and occludin length (**k**,**l**) in the Ctx and Hipp. **m**,**n**, Positive correlation between CypA$^+$ pericytes and MMP9 pericytes in the Ctx (**m**) and Hipp (**n**). Mice (both sexes) were 18–24 months old. Immunostaining for CypA or MMP9 and CD13, ZO-1 and lectin-endothelial staining and/or occludin and lectin-endothelial staining was performed on adjacent sections. In **b** and **h** data are presented as truncated violin plots; continuous line, median; and dotted line, interquartile range. Significance by one-way ANOVA followed by the Tukey post hoc test. In **c**–**f** and **i**–**n**, significance was obtained by by two-tailed simple linear regression. In **c**–**f** and **i**–**n**, the number was based on individual mouse values ($n=10$) for *E4* versus *E3* mice in the absence of *FAD* transgenes (blue-filled and empty circles, respectively) and presence of *FAD* transgenes (red-filled and empty circles, respectively).

5xFAD mice[29,37], in the cortex and hippocampus were not substantially different between 18–24-month-old *APOE4;5xFAD* and *APOE3;5xFAD* mice (Fig. 4a). The tissue analysis confirmed comparable Aβ cortical and hippocampal load in these mice (Fig. 4b,c). As reported[40], Aβ42 levels in female *APOE3;5xFAD* and *APOE4;5xFAD* mice were substantially higher compared to the respective male mice (Fig. 4d). Consistent with previous reports in *5xFAD* lines[29,37], Aβ40 levels in both *APOE4;5xFAD* and *APOE3;5xFAD* mice were substantially lower than Aβ42 levels (Extended Data Fig. 3a). As with Aβ42, we also found substantially higher Aβ40 levels in female

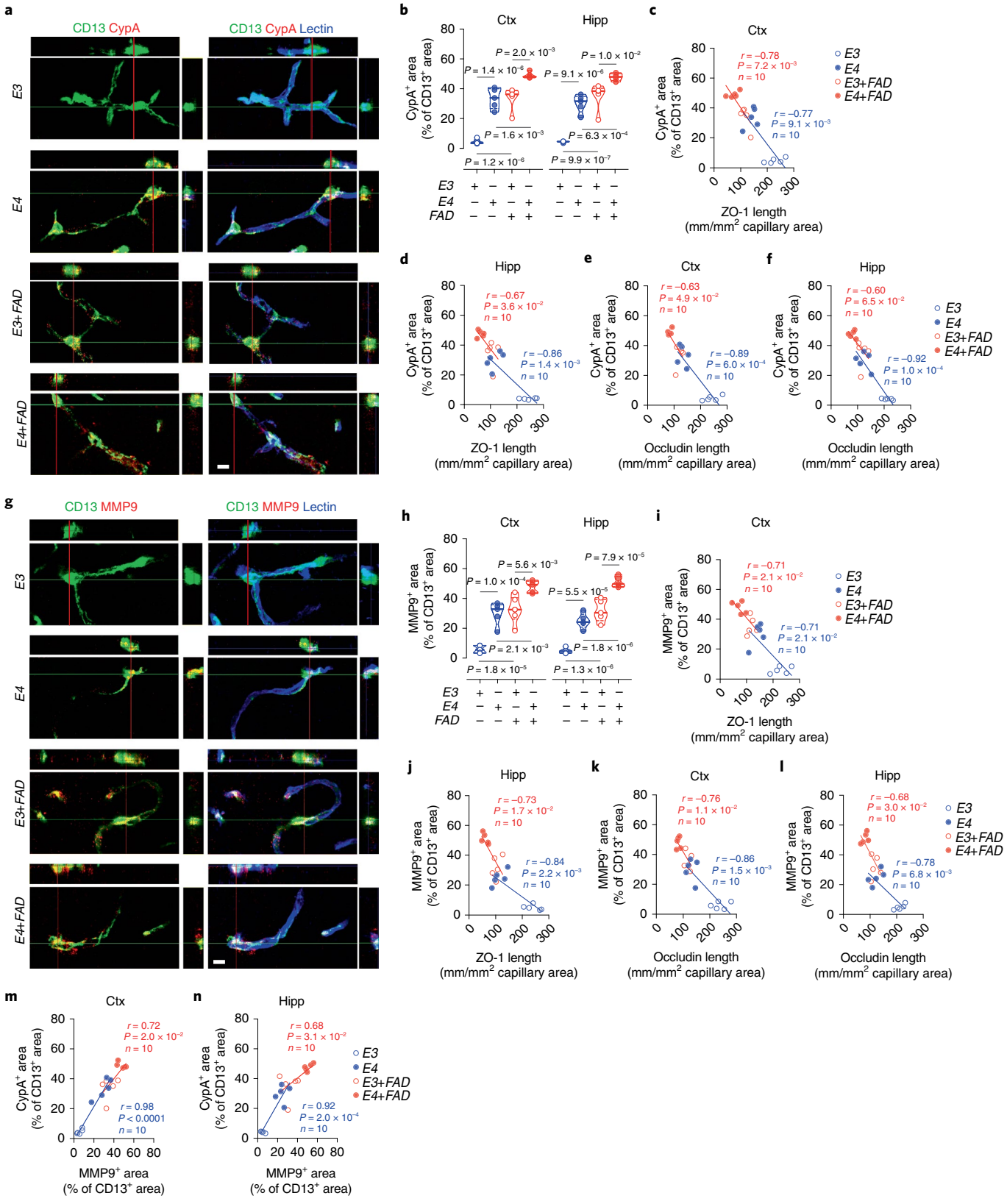

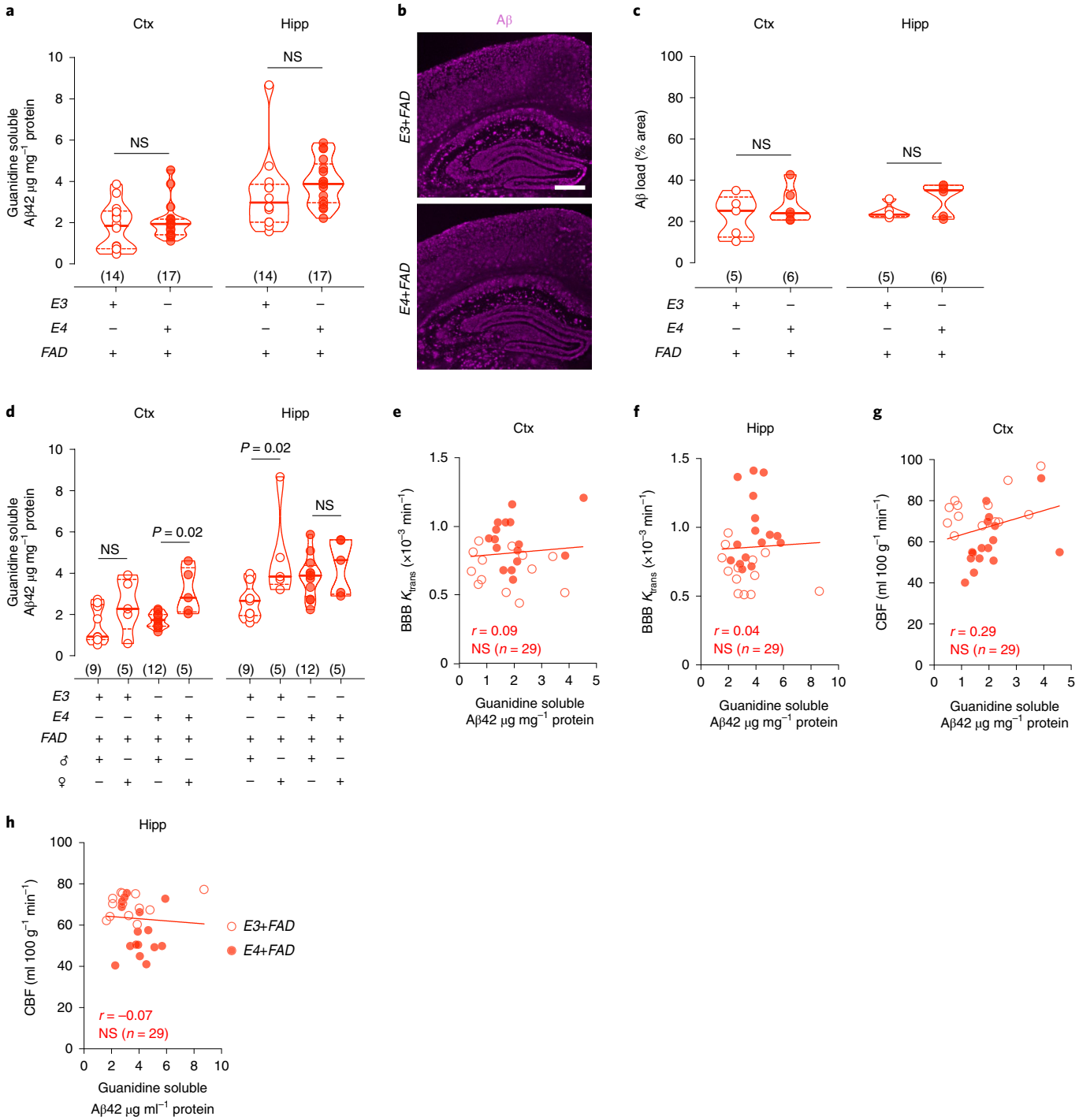

Fig. 4 | Aβ pathology in old *APOE3;5xFAD* and *APOE4;5xFAD* mice and Aβ-independent vascular changes. a, Aβ42 levels in the cortex (Ctx) and hippocampus (Hipp) in *E3+FAD* ($n=14$; red empty circles) and *E4+FAD* ($n=17$; red-filled circles) mice. **b**,**c**, Aβ immunostaining (**b**) and Aβ load in the Ctx or Hipp (**c**) in *E3+FAD* ($n=5$) and *E4+FAD* ($n=6$) mice. Scale bar, 500 μm. **d**, Aβ42 levels in the Ctx and Hipp in male and female *E3+FAD* ($n=14$, 9 ♂ and 5 ♀; red empty circles) and *E4+FAD* ($n=17$, 12 ♂ and 5 ♀; red-filled circles) mice. **e**–**h**, Lack of correlation between the BBB permeability K_{trans} values and Aβ42 levels in the Ctx and Hipp (**e**,**f**) and between regional CBF values and Aβ42 levels in the Ctx and Hipp (**g**,**h**). Mice (both sexes) were 18–24 months old. In **d**–**g**, there were $n=29$ (13 *E3+FAD* and 16 *E4+FAD*) individual mouse data points from both groups. In **a** and **c**, data are presented as violin plots; continuous line, median; and dotted line, interquartile range. Significance was obtained by unpaired two-tailed Student *t*-tests. In **d**, significance was obtained by one-way ANOVA followed by Tukey post hoc test. In **e**–**h**, significance was obtained by two-tailed simple linear regression. NS, not significant.

compared to male mice in both *APOE4* and *APOE3* mice crossed with *5xFAD* mice (Extended Data Fig. 3b).

Interestingly, the increased BBB permeability K_{trans} values and a moderate CBF loss in *APOE4* compared to *APOE3* mice crossed with *5xFAD* mice did not correlate with elevated Aβ42 cortical or hippocampal levels (Fig. 4e–h) or Aβ40 levels (Extended Data Fig. 3e,f), suggesting that Aβ pathology is likely not causing vascular dysfunction in old *APOE4;5xFAD* when compared to *APOE3;5xFAD* mice.

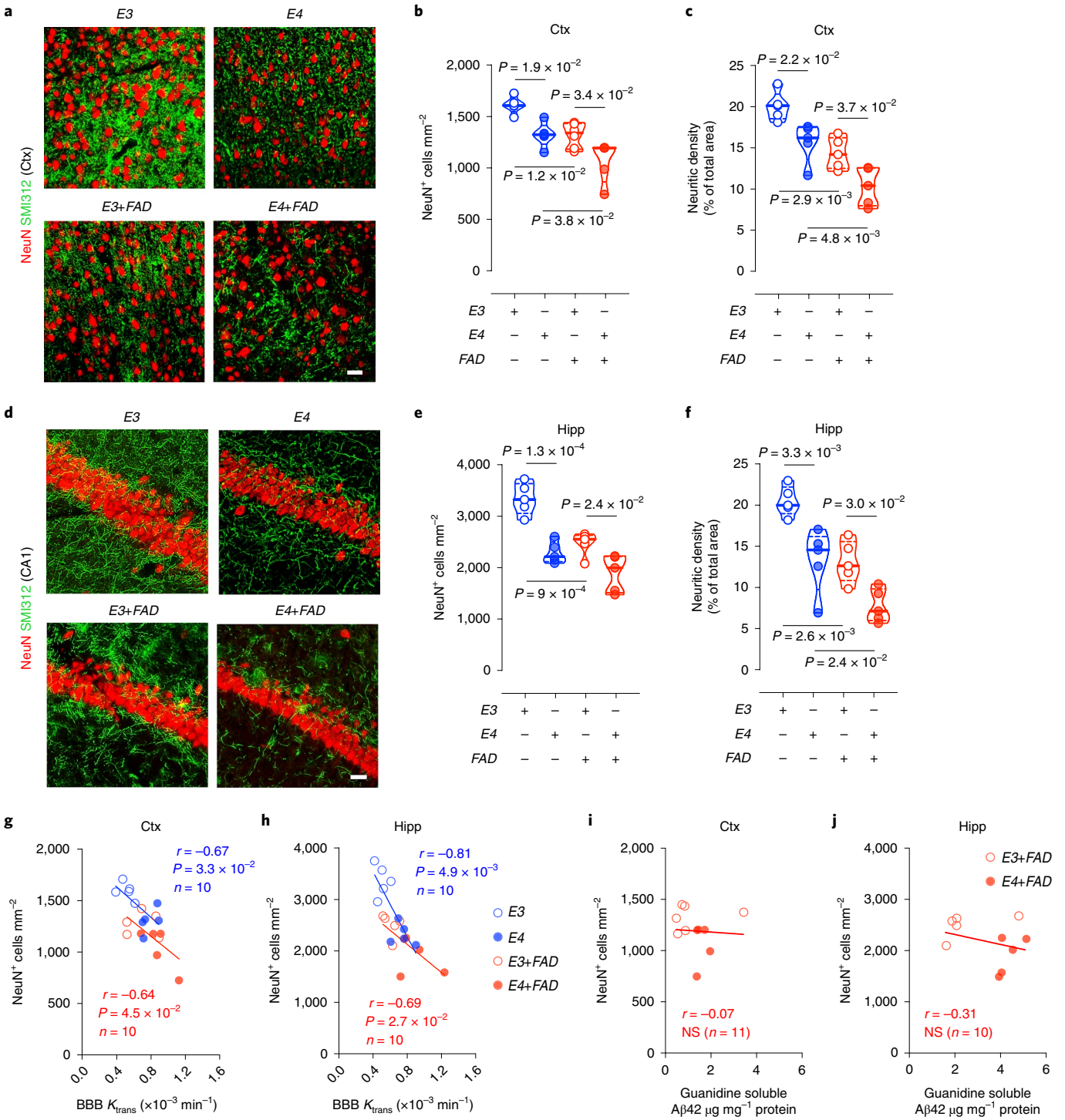

Fig. 5 | Neurodegenerative changes in old *APOE4* and *APOE4;5xFAD* mice correlate with BBB breakdown but not with Aβ pathology. a–f, NeuN$^+$ neurons (red) and SMI312$^+$ neurites (green) and quantification of NeuN$^+$ neurons and SMI312$^+$ neuritic density in the cortex (Ctx) (**a–c**) and hippocampus (Hipp) (**d–f**) in *E3* ($n=5$; blue empty circles), *E4* ($n=5$; blue-filled circles), *E3+FAD* ($n=6$ (**b**); $n=5$ (**c**); $n=5$ (**e**); $n=5$ (**f**); red empty circles) and *E4+FAD* ($n=5$; red-filled circles) mice. Scale bars, 20 μm. **g**,**h**, Negative correlation between the number of NeuN$^+$ neurons and BBB permeability K_{trans} values in the Ctx (**g**) and Hipp (**h**) using individual mouse data points from the studied groups. **i**,**j**, Lack of correlation between the number of NeuN$^+$ neurons and Aβ42 levels in the Ctx (**i**) and Hipp (**j**) in *E3+FAD* ($n=6$ (**i**); $n=5$ (**j**)) and *E4+FAD* ($n=5$ (**i**); $n=5$ (**j**)) individual mouse data points from both groups. Mice (both sexes) were 18–24 months old. In **b**,**c**,**e** and **f**, data are presented as violin plots; continuous line, median; and dotted line, interquartile range. Significance by one-way ANOVA followed by the Tukey post hoc test. In **g–j**, significance was obtained by two-tailed simple linear regression. NS, not significant.

APOE4-mediated neurodegeneration. Next, we found that old *APOE4* mice compared to *APOE3* mice develop accelerated neuron and axon loss without and with Aβ pathology (Fig. 5a–f). This has been shown by 18% and 34% and 11% and 22% loss of neuronal counts and 20% and 27% and 27% and 43% decrease in the neuritic density in the cortex (Fig. 5b,c) and hippocampus (Fig. 5e,f)

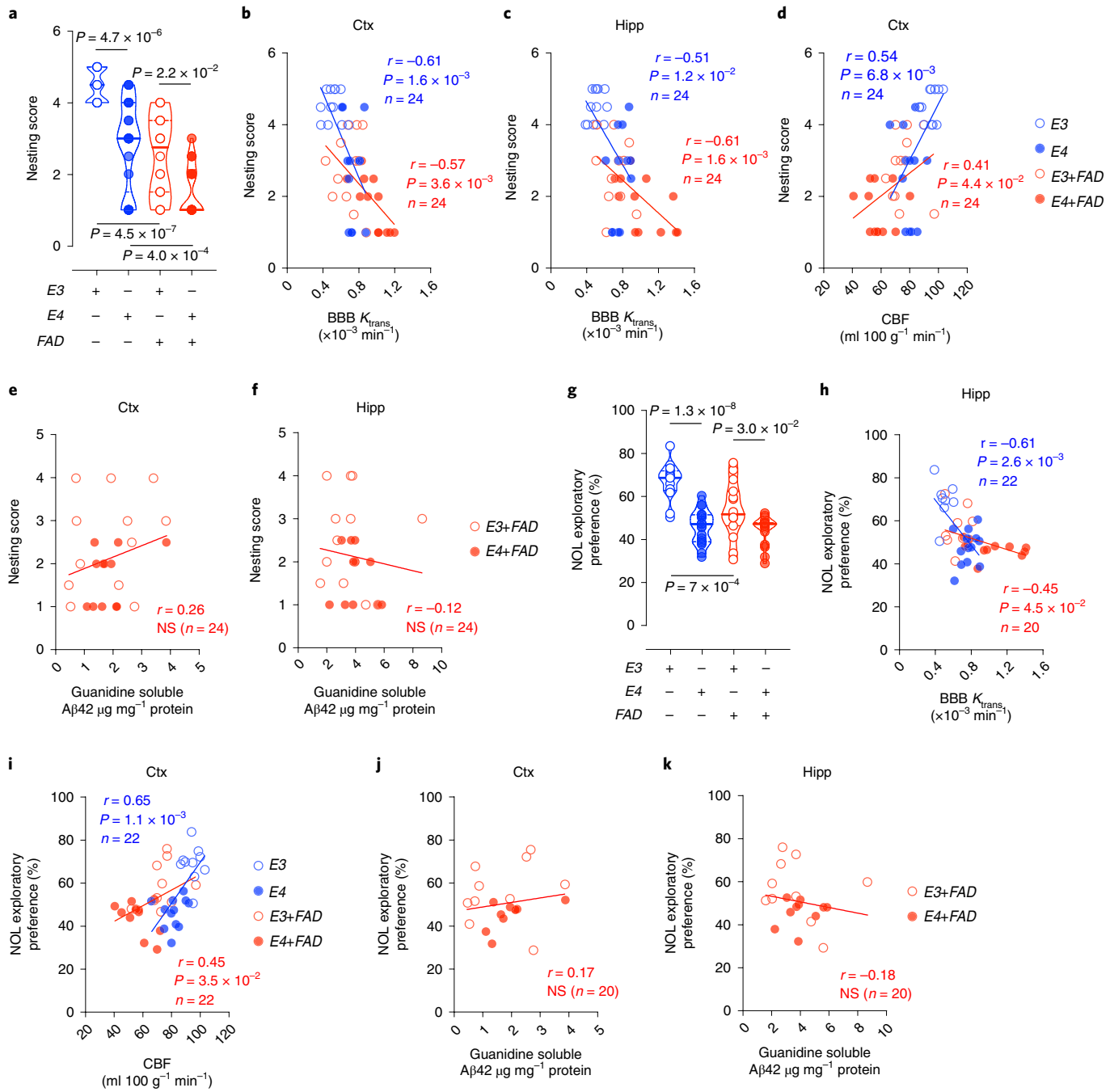

Fig. 6 | Behavioral deficits in old *APOE4* and *APOE4;5xFAD* mice correlate with vascular dysfunction but not with Aβ pathology. a, Nesting scores in *E3* ($n=17$; blue empty circles), *E4* ($n=25$; blue-filled circles), *E3+FAD* ($n=18$; red empty circles) and *E4+FAD* ($n=18$; red-filled circles) mice. **b**,**c**, Negative correlation between nesting scores and BBB permeability K_{trans} values in the cortex (Ctx) (**b**) and hippocampus (Hipp) (**c**). **d**, Positive correlation between nesting scores and CBF values in the Ctx. In **b**–**d**, $n=48$ individual mouse data points from the studied groups. **e**,**f**, Lack of correlation between nesting scores and Aβ42 levels in the Ctx (**e**) and Hipp (**f**); $n=24$ individual mouse data points from the studied groups. **g**, NOL in *E3* ($n=15$), *E4* ($n=21$), *E3+FAD* ($n=15$) and *E4+FAD* ($n=17$) mice. **h**, Negative correlation between NOL and K_{trans} values in Hipp. **i**, Positive correlation between NOL and CBF values in Ctx. In **h** and **i**, $n=42$–44 individual mouse data points from the studied groups. **j**,**k**, Lack of correlation between NOL values and Aβ42 levels in Ctx (**j**) and Hipp (**k**); $n=20$ individual mouse data points from two groups. Mice (both sexes) were 18–24 months old. In **a** and **g**, data are presented as violin plots; continuous line, median; and dotted line, interquartile range. Significance by one-way ANOVA followed by the Tukey post hoc test. In **b**–**f** and **h**–**k**, significance was obtained by two-tailed simple linear regression. NS, not significant.

in *APOE4* versus *APOE3* control mice alone and in these mice crossed with *5xFAD* mice, respectively. Consistent with previous reports showing early neuronal dysfunction in *APOE4* transgenic lines[3] and in *5xFAD* mice showing neuron and synaptic loss[29,39], we found substantial 17% and 23% and 10% and 10% reduction in neuronal counts and 30% and 37% and 36% and 51% reduction in neuritic density in the cortex and hippocampus of *5xFAD;APOE3* and *5xFAD;APOE4* mice compared to their respective *APOE3* and *APOE4* knock-in littermate controls (Fig. 5b,c,e,f). Notably, loss of neurons correlated with the increased BBB K_{trans} values reflecting

BBB breakdown (Fig. 5g,h), but did not correlate with elevated Aβ42 levels (Fig. 5i,j).

APOE4-related behavioral deficits. Finally, we found that *APOE4* compared to *APOE3* mice develop behavioral deficits on daily activity tests as shown by a substantial drop in the nest construction score both in the presence and absence of Aβ pathology (Fig. 6a). A drop in the nesting scores correlated with the increased BBB K_{trans} values and diminished CBF (Fig. 6b–d), but did not correlate with elevated Aβ42 levels in the cortex or hippocampus (Fig. 6e,f). *APOE4* compared to *APOE3* mice also developed hippocampal-associated memory deficits as shown by their worse performance on the novel object location (NOL) test both in the presence and absence of Aβ pathology (Fig. 6g). Deficits in NOL exploratory preference correlated with the increased BBB permeability K_{trans} values in the hippocampus (Fig. 6h) and diminished CBF in the cortex (Fig. 6i), but not with elevated Aβ42 levels in either of these regions (Fig. 6j,k).

Inhibition of the CypA-MMP9 pathway in *APOE4;5FAD* mice. Next, we treated 10–12-month-old *APOE4;5xFAD* and *APOE3;5xFAD* mice with a non-immunosuppressive CypA inhibitor Debio-025, which has been used in humans for non-neurological indications such as hepatitis C[46]. Additionally, Debio-025 is currently undergoing testing for SARS-CoV-2 infection[47] and is in phase 2 clinical trial against COVID-19 (www.clinicaltrialsarena.com/news/debiopharm-begins-alisporivir-france).

Debio-025 was administered for 30 d (10 mg kg^{-1} d^{-1} intraperitoneally (i.p.)) using a dosing regimen as previously reported in mouse models of muscular dystrophy and myopathy[48,49] and in the low-density lipoprotein receptor-related protein 1 (LRP1) endothelial-specific knockout mice[50]. We started Debio-025 at 10–12 months of age, when *APOE4;5xFAD* compared to *APOE3;5xFAD* mice develop accelerated BBB breakdown, behavioral deficits and substantial loss of neuronal networks, as reported[42,51] (Fig. 7a) The goal of this experiment was to determine whether protecting BBB integrity by suppressing the CypA-MMP9 pathway in pericytes can prevent further neuron loss and behavioral changes in *APOE4;5xFAD* relative to *APOE3;5xFAD* mice.

Immunocytochemical analysis indicated that a 30-d treatment with Debio-025 compared to vehicle substantially reduced CypA$^+$ and MMP9$^+$ immunofluorescent signal in CD13$^+$ pericytes in the cortex and hippocampus of *APOE4;5xFAD* mice down to the levels seen in *APOE3;5xFAD* mice, respectively (Fig. 7b–e). Consistent with inhibition of the CypA-MMP9 BBB-degrading pathway[3], treatment of *APOE4;5xFAD* mice with Debio-025 increased the length coverage of tight junction proteins ZO-1 and occludin that are both well-known substrates for enzymatic degradation by MMP9 (ref. [3]) (Fig. 7f–i). However, Debio-025 did not have an effect on CypA$^+$ and/or MMP9$^+$ signal in CD13$^+$ pericytes, nor on ZO-1 and occludin length in *APOE3;5xFAD* mice. Inhibition of the CypA-MMP9 pathway in *APOE4;5xFAD* mice improved BBB integrity as shown in vivo by DCE-MRI (Fig. 7) and ex vivo by reduced perivascular capillary fibrinogen deposits (Fig. 7g) and was associated with improved pericyte coverage (Fig. 7h,i).

We then found that Debio-025 compared to vehicle prevented further loss of neurons and axon density in the cortex and hippocampus of *APOE4;5xFAD* mice (Fig. 8a–c) and improved performance on NOL and novel object recognition (NOR) hippocampal tests (Fig. 8d,e) bringing them nearly to the levels seen in *APOE3;5xFAD* mice, but did not have an effect on neuronal phenotype or behavior in *APOE3;5xFAD* mice. Notably, age-matched *APOE3* control mice not expressing *5xFAD* transgenes had still notably higher neuronal counts, neuritic density and better performance on hippocampal NOR test than Debio-025-treated *APOE4;5xFAD* mice or *APOE3;5xFAD* mice (Extended Data Fig. 4). These data suggest that Debio-025 ameliorates *APOE4*-mediated loss of neurons and behavioral deficits relative to *APOE3*, but does not protect against neurodegenerative changes caused by *5xFAD* transgenes and subsequent direct Aβ neurotoxicity, as previously shown in *5xFAD* mice[29,37,52]. Consistent with these findings, Debio-025 had no effect on Aβ42 or Aβ40 levels in the cortex and hippocampus of *APOE4;5xFAD* or *APOE3;5xFAD* mice (Fig. 8f,g), confirming that protection of neuronal phenotype in *APOE4;5xFAD* mice is independent of Aβ pathology.

Discussion

Our findings show that old *APOE4* knock-in mice and *APOE4;5xFAD* mice, compared to their respective *APOE3* lines develop an accelerated BBB breakdown associated with loss of pericyte capillary coverage and reductions in CBF associated with diminished capillary density both in the presence and absence of Aβ. Tissue analysis revealed reductions in the tight junction proteins ZO-1 and occludin coverage length, which correlated with activation of the CypA-MMP9 BBB-degrading pathway in pericytes. As previously reported, this pathway is activated in pericytes in transgenic *APOE4* lines[3], as well as at the BBB endothelial cells and pericytes in human *APOE4* AD carriers as shown by postmortem tissue analysis[2] and in living *APOE4* carriers, as shown by cerebrospinal fluid analysis[17]. When activated, the CypA-MMP9 pathway leads to MMP9-mediated enzymatic degradation of the BBB tight junction proteins causing BBB breakdown[3,50].

Fig. 7 | Debio-025 inhibits the CypA-MMP9 pathway in pericytes and improves BBB integrity in *APOE4;5xFAD* mice. a, A schematic of the time course of Debio-025 experiment. **b**, Confocal images of CD13$^+$ pericytes (green), CypA (red) and lectin$^+$ endothelium (blue) in the cortical capillaries in *E4+FAD* mice treated with vehicle or Debio-025. Orthogonal views, colocalization of CypA with CD13$^+$ pericytes; scale bar, 10 μm. **c**, Quantification of CypA$^+$ pericytes in the cortex (Ctx) and hippocampus (Hipp) in *E3+FAD* (red empty circles) and *E4+FAD* (red-filled circles) mice treated with vehicle or Debio-025; $n=5$ mice per group. **d,** Confocal images of CD13$^+$ pericytes (green), MMP9 (red) and lectin$^+$ endothelium (blue) in cortical capillaries in *E4+FAD* mice treated with vehicle or Debio-025. Orthogonal views, colocalization of MMP9 with CD13$^+$ pericytes; scale bar, 10 μm. **e**, Quantification of MMP9$^+$ pericytes in the Ctx and Hipp in *E3+FAD* (red empty circles) and *E4+FAD* (red-filled circles) mice treated with vehicle or Debio-025; $n=5$ mice per group. **f**,**g** Immunostaining for ZO-1 (red) and lectin$^+$ endothelium (blue) in the Ctx in *E4+FAD* mice treated with vehicle or Debio-025 (**f**, red) and ZO-1 length in the Ctx and Hipp (**g**) in *E3+FAD* (red empty circles) and *E4+FAD* (red-filled circles) mice treated with vehicle or Debio-025; $n=5$ mice per group; scale bar, 20 μm. **h–i**, Immunostaining for occludin (green) and lectin$^+$ endothelium (blue) in the Ctx (**h**, green) and occludin length in the Ctx and Hipp (**i**) in *E3+FAD* (red empty circles) and *E4+FAD* (red-filled circles) mice treated with vehicle or Debio-025; $n=5$ mice per group; scale bar, 20 μm. Boxes in **f** and **h** denote sites taken for higher magnification insets shown below merged images. **j**, BBB permeability K_{trans} values in the Ctx and Hipp in *E3+FAD* vehicle-treated ($n=6$; red empty circles), *E3+FAD* Debio-025-treated ($n=8$; red empty circles), *E4+FAD* vehicle-treated ($n=8$; red-filled circles) and *E4+FAD* Debio-025-treated ($n=8$; red-filled circles) mice. **k**, Quantification of fibrinogen$^+$ pericapillary deposits in the Ctx and Hipp in *E3+FAD* (red empty circles) and *E4+FAD* (red-filled circles) mice treated with vehicle or Debio-025; $n=5$ mice per group. **l**,**m**, CD13$^+$ pericyte coverage (magenta) of lectin$^+$ endothelial capillary profiles (blue) in the Ctx (**l**; scale bar, 20 μm) and quantification of pericyte capillary coverage in the Ctx and Hipp (**m**) in *E3+FAD* (red empty circles) and *E4+FAD* (red-filled circles) mice treated with vehicle or Debio-025; $n=5$ mice per group (scale bar, 20 μm). Mice (both sexes) were 10–12 months old. In **c**,**e**,**g**,**i–k** and **m** data are presented as truncated violin plots; continuous line, median; and dotted line, interquartile range. Significance was determined by one-way ANOVA followed by the Tukey post hoc test.

As recently reported[40], we found comparable Aβ pathology in old *APOE3;5xFAD* and *APOE4;5xFAD* mice, but with higher severity in females than in males in both genotypes. Notably, elevated Aβ42 levels, the major Aβ species in *5xFAD* mice[29,30,37,40] and of Aβ40, did not correlate with BBB breakdown or CBF reductions in these mice, suggesting that *APOE4*-mediated vascular dysfunction in old mice

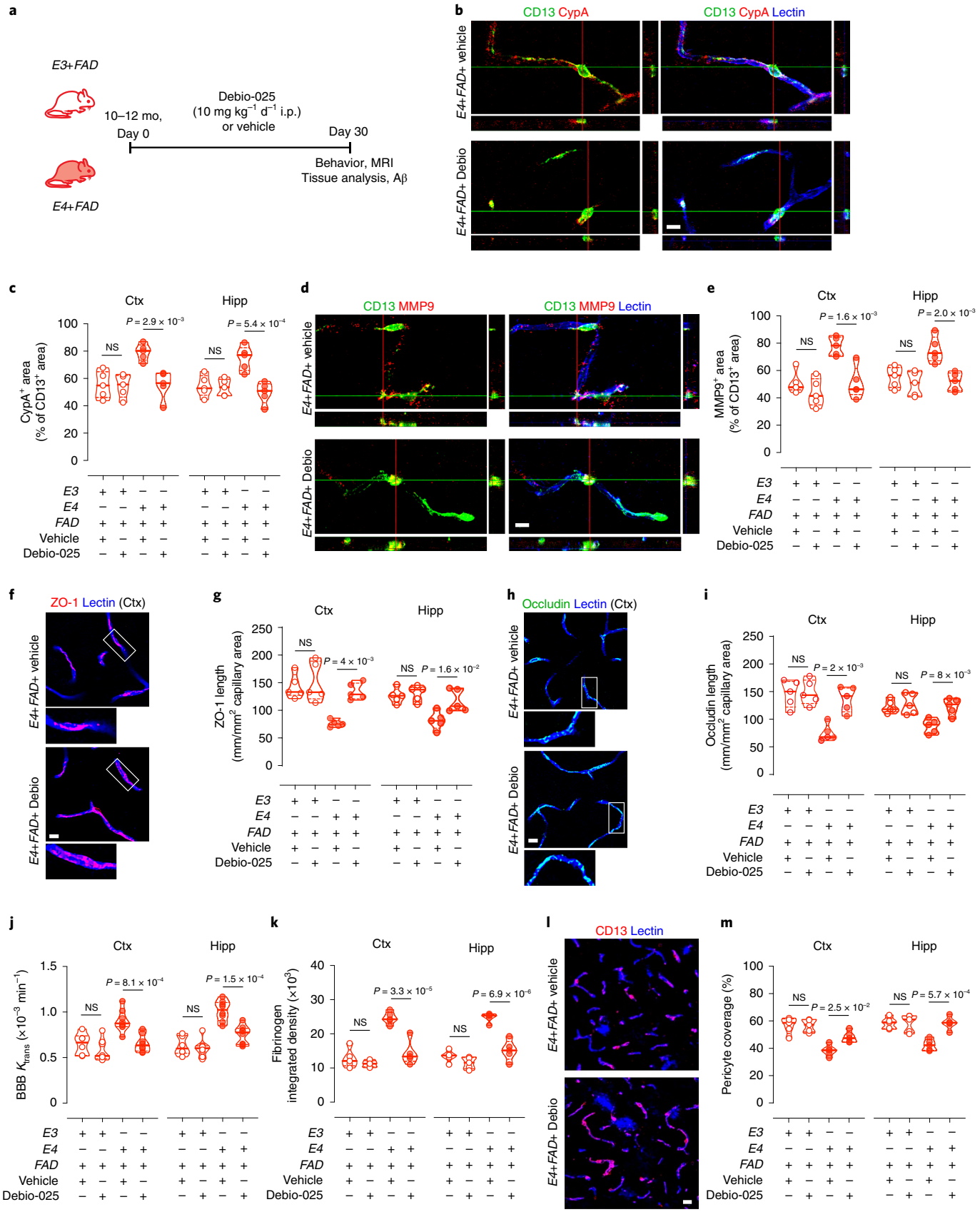

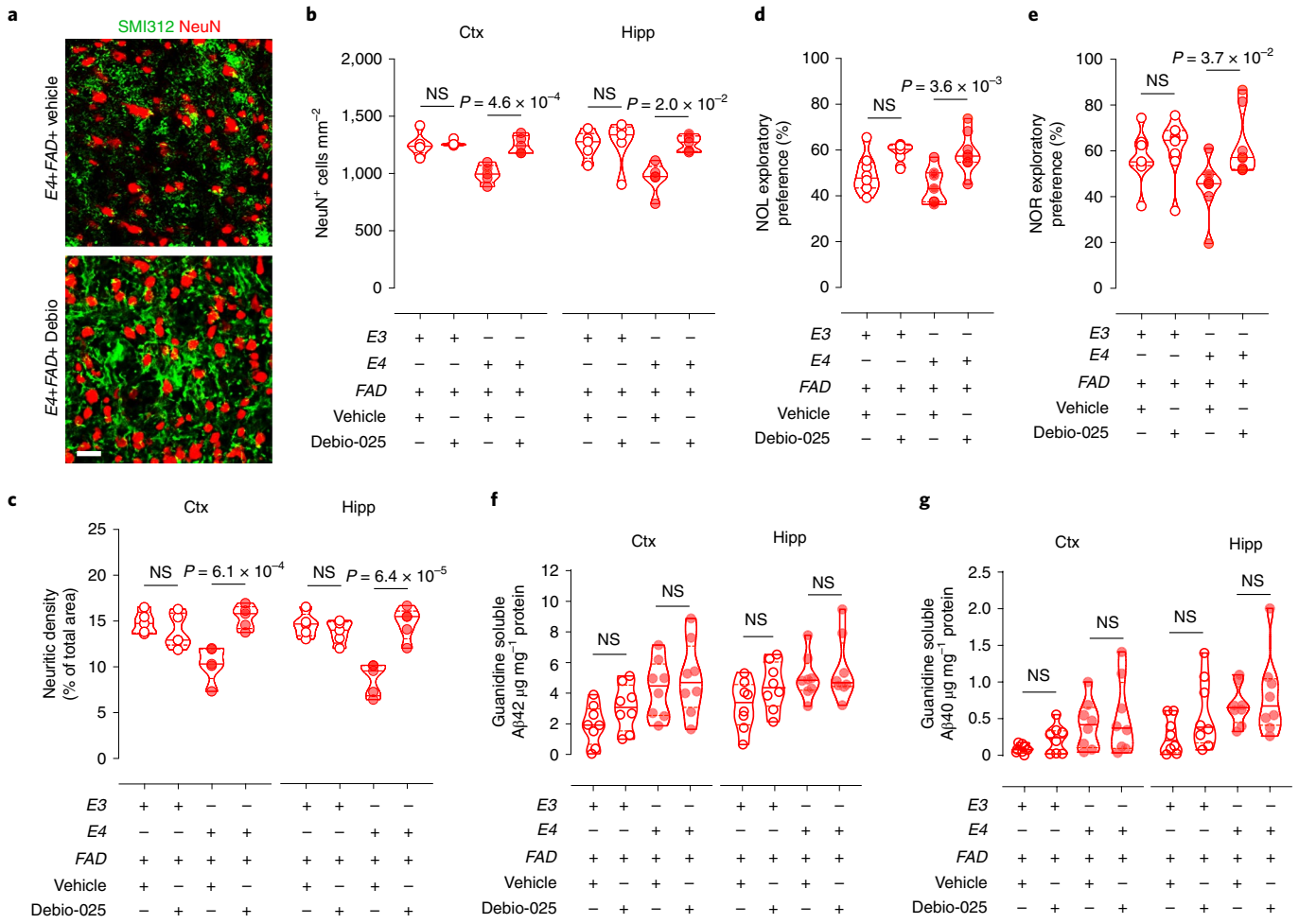

Fig. 8 | Debio-025 prevents further loss of neurons and improves cognitive function in *APOE4;5xFAD* mice without affecting Aβ42 or Aβ40 levels in the brain. a–c, Cortical NeuN+ neurons (red) and SMI312+ neurites (green) (**a**) and quantification of NeuN+ neurons (**b**) and SMI312+-neuritic density (**c**) in the cortex (Ctx) and hippocampus (Hipp) in *E3+FAD* (red empty circles) and *E4+FAD* (red-filled circles) mice treated with vehicle or Debio-025; $n = 5$ mice per group. Scale bar, 20 µm. **d**,**e**, NOL (**d**) and NOR (**e**) in *E3+FAD* vehicle-treated ($n = 8$; red empty circles), *E3+FAD* Debio-025-treated ($n = 9$; red empty circles), *E4+FAD* vehicle-treated ($n = 7$; red-filled circles) and *E4+FAD* Debio-025-treated ($n = 8$; red-filled circles) mice. **f**,**g**, Aβ42 (**f**) and Aβ40 (**g**) levels in the Ctx and Hipp in *E3+FAD* vehicle-treated ($n = 8$; red empty circles), *E3+FAD* Debio-025-treated ($n = 8$; red empty circles), *E4+FAD* vehicle-treated ($n = 8$; red-filled circles) and *E4+FAD* Debio-025-treated ($n = 8$; red-filled circles) mice. Mice (both sexes) at 10–12 months old were the same as in Fig. 7. In **b**–**g**, data are presented as violin plots; continuous line, median; and dotted line, interquartile range. Significance was obtained by one-way ANOVA followed by Tukey post hoc test.

is Aβ-independent. Moreover, neuron loss and behavioral deficits in *APOE4* compared to *APOE3* lines correlated well with losses in BBB integrity and CBF, but not with Aβ pathology, as indicated by the lack of correlation between neuron loss and Aβ42 levels, or behavioral deficits and Aβ42 levels.

Loss of neurons and neuritic density in *5xFAD* mice crossed with *APOE3* and *APOE4* mice is consistent with findings of neuron and synaptic loss in older *5xFAD* mice, as reported[29,39]. Strong correlation between BBB dysfunction and neurodegenerative and behavioral changes in *APOE4* compared to the respective *APOE3* lines, is consistent with enhanced brain capillary leakages of blood-derived neurotoxic proteins such as albumin[53], thrombin, plasminogen and/or iron-containing proteins[3,5] or fibrinogen[41], all capable of causing neuron and synaptic dysfunction and/or eventually neuron death by different but complementary mechanisms. Additionally, greater pericyte loss in *APOE4* compared to *APOE3* lines in the absence and presence of Aβ pathology results in a greater loss of pericyte-derived neurotrophic growth factors, such as pleiotrophin[6], which might further accelerate neuron loss particularly in the presence of diminished CBF, as we recently reported[6].

How different AD pathologies interact to contribute to an advanced AD disease stage with age has been understudied and poorly understood. The present findings indicate that vascular dysfunction, particularly the BBB breakdown, plays a important role accelerating neurodegenerative process and cognitive impairment in old Alzheimer's mice independently of Aβ and therefore it could be an important new therapeutic target for treating an advanced disease stage for which anti-Aβ strategies have proven to be ineffective. Indeed, treatment of *APOE4;5xFAD* mice with CypA inhibitor Debio-025 suppressed the CypA-MMP9 pathway in pericytes, which in turn improved BBB integrity and prevented further neuron loss and behavioral deficits despite having no effect on Aβ pathology. These results suggest that interventions directed at the BBB repair and improvement of vascular dysfunction are potentially viable new approaches to slow down and/or arrest neurodegenerative process and cognitive decline in an advanced AD stage. As Debio-025 has been used in humans for non-neurological applications[46] this approach may hold potential to treat cognitive impairment in *APOE4* carriers that show activation of the CypA-MMP9 pathway in the cerebrospinal at an early disease stage[17] and at the

BBB at a later disease stage with fully developed AD as shown by neuropathological analysis[2].

One limitation of the present Debio-025 experiment, however, is that it has been performed in somewhat younger 10–12-month-old *APOE4;5xFAD* and *APOE3;5xFAD* mice, compared to the rest of the study that has been carried out in older 18–24-month-old mice. Although, at 10–12 months of age *APOE4;5xFAD* compared to *APOE3;5xFAD* mice develop accelerated BBB breakdown, behavioral deficits and notable loss of neuronal networks[42,51] and both genotypes develop substantial Aβ pathology[30,40], as we have also demonstrated, it remains to be seen whether Debio-025 treatment will have similar striking effects in 18–24-month-old mice. This, however, is a challenging experiment because of increased mortality of *APOE4;5xFAD* mice at that old age as reported[40] and as we also observed.

Our data show that activation of the CypA-MMP9 pathway leads to reductions in tight junction proteins causing BBB breakdown in *APOE4* and *APOE4;5FAD* mice, but whether nonspecific caveolar transcytosis is also affected by *APOE4*, as in some other models of BBB breakdown[54], remains presently unknown and should be addressed by future studies. It has been also reported that epidermal growth factor (EGF) can increase capillary length and improve BBB permeability in *APOE4;5FAD* mice[42], but whether the EGF–EGFR signaling pathway can play a role in spontaneous BBB breakdown as observed in *APOE4;5FAD* mice has not been studied. Additionally, future studies should address at the cellular and molecular level how *APOE4* leads to CBF reductions and whether loss of CBF is related to loss in pericyte coverage and/or reductions in microvascular density, as suggested by our correlation data and/or is caused by activation of the CypA-MMP9 pathway in pericytes or alternatively by a different underlying mechanism.

The present study confirms that Aβ pathology increases BBB breakdown and CBF deficits in *APOE3;5xFAD* mice compared *to APOE3* control mice, which is to be expected given that *5xFAD* mice alone develop BBB breakdown[34–37] and CBF deficits[38], as a result of direct Aβ vasculotoxicity. Interestingly, we also found activation of the CypA–MMP9 pathway in pericytes in *APOE3;5xFAD* mice relative to *APOE3* control mice. Whether this could be attributed to direct toxic effects of Aβ on pericytes[43] and/or to Aβ-mediated proteasomal degradation of LRP1[55] resulting in loss of this receptor which is required for suppression of the CypA–MMP9 pathway by apoE3 (ref. [3]), remains to be determined by future studies. Namely, studies in pericyte cultures and transgenic mice show that apoE3 requires LRP1 to maintain CypA synthesis within low physiological range, whereas poor interaction of apoE4 with LRP1 in pericytes leads to activation of this pathway via transcriptional activation of CypA triggering NF-κB transcriptional activation of MMP9, which increases active MMP9 levels degrading BBB tight junction proteins[3]. Furthermore, silencing LRP1 in vivo in *APOE3* knock-in mice blocks apoE3-mediated suppression of CypA leading to activation of the CypA–MMP9 pathway and BBB breakdown similarly as seen in *APOE4* mice[3]. As LRP1 is reduced in blood vessels in AD in humans[2,55–57] and in AD Aβ models[55,58–60], it is possible that LRP1 loss from blood vessels and pericytes may contribute to activation of the CypA–MMP9 pathway in *APOE3;5xFAD* mice.

In conclusion, our findings show that *APOE4* accelerates advanced-stage vascular dysfunction, BBB breakdown and neurodegeneration in AD mice via the CypA pathway in pericytes independently of Aβ. These findings have implication not only for better understanding the pathogenesis of an advanced-stage vascular and neurodegenerative disorder in AD, but also for potential treatment of *APOE4* carriers with advanced AD for whom we do not have yet an effective apoE-based therapy to offer.

Methods

Animals. As previously described[30], *APOE3;5xFAD* and *APOE4;5xFAD* mice, also commonly called *E3FAD* and *E4FAD* mice, respectively, were generated by crossing heterozygous *5xFAD*$^{\pm}$ line (Tg6799 on a C57BL/6 and SJL background) that coexpress five FAD mutations (*APP* K670N/M671L, I716V, V717I and *PS1* M146L, L286V) under the control of the neuron-specific mouse Thy-1 promoter[29] with homozygous human *APOE3*$^{+/+}$ and *APOE4*$^{+/+}$ targeted replacement mice (on C57BL/6 background)[28]. *APOE3;5xFAD* and *APOE4;5xFAD* littermate controls or noncarriers derived from these litters were *5xFAD*$^{-/-}$*;APOE3*$^{+/+}$ and *5xFAD*$^{-/-}$*;APOE4*$^{+/+}$, respectively, which we refer to as *APOE3* and *APOE4* knock-in control mice. Breeding pairs were generously provided by M. J. LaDu (University of Illinois at Chicago).

This study used both male and female mice at 18–24 months of age. The survival rate of mice at age 18 months was 90% and 80% for *APOE3* and *APOE4* knock-in littermate controls and 75% and 55% for *APOE3;5xFAD* and *APOE4;5xFAD* lines and was driven by early death of female *APOE4* mice, as previously shown[40]. All survivors between 18 and 24 months of age were used in the study. Group sizes varied from $n=12$–16 for MRI studies, $n=17$–25 for behavioral studies, $n=14$–17 for Aβ assays and $n=5$–6 for tissue immunohistology analysis for all four groups *APOE3*, *APOE4*, *APOE3;5xFAD* and *APOE4;5xFAD*. All procedures were approved by the Institutional Animal Care and Use Committee at the University of Southern California using US National Institutes of Health guidelines. All animals were randomized for their genotype information and were included in the study. The operators responsible for experimental procedure and data analysis were blinded and unaware of group allocation throughout the experiments.

Treatment with Debio-025. Debio-025 (MedChem Express, cat. no. HY-12559), a non-immunosuppressive CypA inhibitor, was administered in 10–12-month-old *APOE3;5xFAD* and *APOE4;5xFAD* mice generated as above ($n=7$–11 per group as indicated in Fig. 8 legend) at 10 mg kg^{-1} d^{-1} i.p. for 30 d following a dosing regimen as previously reported in mouse models[48–50]. Control mice received vehicle for 30 d. NOL and NOR behavioral tests were performed 30 d after Debio-025 or vehicle treatment before the DCE-MRI study. Mice were killed after 30 d and brains collected for tissue analysis.

Magnetic resonance imaging. As we previously reported[6,41], mice were scanned with either a Biospec 7T system (300 MHz, Bruker) at the California Institute of Technology or a MR Solutions 7T positron emission tomography–MR system (MR Solutions Ltd.) at the Zilkha Neurogenetic Institute (University of Southern California). The Bruker system was equipped with the standard B-GA12 gradient set (~114-mm inner diameter; 400 mT.m^{-1} maximum gradient) and a 35-mm internal diameter quadrature volume coil (M2M Imaging). The MR Solutions system was equipped with the MRS cryogen-free MRI system (bore size ~24 mm, up to 600 mT.m^{-1} maximum gradient) and a 20-mm internal diameter quadrature bird cage mouse head coil. Comparable sequences and parameters were used with both MR scanners, as described below.

As we previously reported[6,41], mice were anesthetized by 1–1.5% isoflurane/air. Respiration rate (80 ± 10 breaths min^{-1}) and body temperature (36.5 ± 0.5 °C) were monitored during the experiments using an abdominal pressure-sensitive probe and a rectal temperature probe. The isoflurane dose and heated air flow was adjusted continuously to ensure stable and reproducible depth of anesthesia. The sequences were collected in the following order: T2-weighted (two-dimensional-fast spin echo, TR/TE 4,900/45 ms, 34 slices, slice thickness 500 µm, in-plane resolution 70 × 70 µm^2) to obtain structural images; DCE protocol for the BBB permeability assessment; and finally, DSC imaging for CBF. Total imaging time was approximately 40 min per mouse.

As we previously reported[6,41], DCE-MRI imaging protocol was performed within the dorsal hippocampus territory and included measurement of pre-contrast T1-values using a variable flip angle fast low-angle shot (FLASH) sequence (FA = 5, 10, 15, 30 and 45°, TR/TE = 18 ms/4 ms, slice thickness 1 mm, in-plane resolution 85 × 85 µm^2), followed by a dynamic series of 325 T1-weighted images with identical geometry and a temporal resolution of 4.6 s (FLASH, TR/TE 18 ms/4 ms, flip angle 15°, slice thickness 1 mm, in-plane resolution 85 × 85 µm^2). Using a power injector, a bolus dose (140 µl) of 0.5 mmol kg^{-1} gadolinium-diethylenetriamine pentaacetic acid (Gd-DTPA), BioPAL, Inc., diluted in saline 1:6) was injected via the tail vein at a rate of 600 µl min^{-1}. DCE images were collected for 5 min before and 20 min after the injection. DSC-MRI imaging was performed on the exact same geometry. A dynamic series of 100 T2*-weighted images was used, with a temporal resolution of 1.5 s (FLASH, TR/TE 18 ms/4 ms, slice thickness 1 mm, flip angle 15°, in-plane resolution 170 × 270 µm^2). A second bolus dose (140 µl) of Gd-DTPA (1:1) was injected via the tail vein at a rate of 1,000 µl min^{-1}. DSC images were collected over 120 s after the injection.

MRI analysis. *T1 mapping.* As we described previously[6,41], T1 relaxation times were estimated using the variable flip angle method, before Gd-DTPA injection, with a series of FLASH images with varying FA and constant TR and TE using the standard saturation recovery equation.

Blood–brain barrier permeability. As we previously reported[6,41], post-processing of the collected DCE-MRI data was performed using in-house DCE processing software (Rocketship) implemented in Matlab[61]. The unidirectional blood-to-

brain transfer constant, K_{trans}, to intravenously injected gadolinium-based contrast agent was determined in both primary somatosensory cortex and hippocampus in mice using a modified method, as previously reported in both humans[17,23,26] and mice[6,41] with the post-processing Patlak analysis[62]. As reported previously[6,17,23,26,41], we determined the arterial input function (AIF) in each mouse from the common carotid artery.

As we previously reported[6,41], the total tracer concentration in the tissue, $C_{tissue}(t)$, can be described as a function of the arterial vascular concentration $C_{AIF}(t)$, the intravascular blood volume v_p and the BBB permeability transfer constant K_{trans} that represents the flow of the tracer from the intravascular to the extravascular space using equation (1) below.

$$C_{\text{tissue}}(t) = K_{\text{trans}} \int_0^t C_{\text{AIF}}(\tau)\, d\tau + v_p \cdot C_{\text{AIF}}(t) \quad (1)$$

Cerebral blood flow. As reported previously, DSC-MRI data were processed using our in-house Matlab code[6,41,63]. In brief, assuming a linear relationship between the signal drop induced by Gd-DTPA and concentration, these quantities can be related via:

$$S(t) = S_0 \times e^{-r_2 * .C(t).\text{TE}} \quad (2)$$

Where $S(t)$ is the signal intensity at time t after bolus injection for any given voxel, S_0 is the mean pre-contrast signal intensity, r_2* relaxivity constant of the contrast agent used, $C(t)$ is the concentration of contrast as a function of time and TE is the time echo of the acquisition sequence. From the previous formula, the conversion from signal to contrast agent concentration is straightforward and occurs via:

$$C(t) = \frac{-1}{r_{2*}.\text{TE}} \ln\left(\frac{S(t)}{S_0}\right) \quad (3)$$

As we previously reported[6,41], the profile of this concentration curve is heavily influenced by the manner in which the tracer bolus is injected into the mouse. To define the shape of the bolus curve, a representative AIF was obtained for each mouse individually. The AIF was obtained from the image data via manual delineation, typically from the common carotid arteries (same as for K_{trans} mapping). By defining the residual function, R(t), which represents the fraction of tracer presently circulating at time t, the relationship between tracer concentration and blood flow can be modeled as a convolution between R(t) and the AIF:

$$C_t(t) = \frac{\rho}{Kh} F \int_0^t C_a(\tau)\, R(t-\tau)\, d\tau \quad (4)$$

Where $C_t(t)$ is the concentration of contrast agent in the tissue, F is regional CBF, κ_H is the ratio of capillary to artery hematocrit (a value of 0.45 was used), ρ is tissue density (1.04 g ml^{-1}), $C_a(t)$ is AIF time course. To solve equation (4), we evoked an oscillation-limited circulant singular value decomposition approach[64]. Using this deconvolution, R(t) and F values were obtained and regional CBF (ml 100 g^{-1} min^{-1}) was computed using the equation:

$$\text{CBF} = \frac{\kappa_H}{\rho} . \max(R(t)) \quad (5)$$

Behavior. *Nesting.* Nest construction test was performed as previously reported[41,43,59]. Two hours after the beginning of the dark cycle, the animals were individually placed in clean home cages with a single nestlet. Nests were assessed the next morning and evaluated following the five-point scale as we described in detail[59].

Novel object location. This was performed as we have previously reported[5,6,43]. Briefly, animals were placed in a 30-cm^3 box and allowed to habituate to the testing area for 10 min. Animals were then placed back in their cages and two identical approximately 5 × 5-cm objects were placed in the top left and right corner of the testing area. Animals were allowed to explore the two objects in the testing area for 5 min before being returned to their cages. After a 1-h interval one of the objects was relocated and the animals were allowed to explore the testing area once again for 3 min. After each trial, the testing area and the objects were thoroughly cleaned with 70% ethanol solution. All the trials, including habituation, were recorded with a high-resolution camera and the amount of time each animal spent exploring the objects was analyzed. Any animals that presented a preference for either of the two identical objects, before replacement with the novel location, were eliminated from the analysis.

Immunohistochemistry. As we previously reported[6,41], mice were anesthetized i.p. with 100 mg kg^{-1} ketamine and 10 mg kg^{-1} xylazine and transcardially perfused with 20 ml phosphate-buffered saline (PBS) containing 5 mM ethylenediaminetetraacetic acid (EDTA). Brains were removed, snap-frozen and one hemisphere was embedded into OCT compound (Tissue-Tek) on dry ice (the other hemisphere was used for biochemical assays; see Human Aβ40 and Aβ42 specific ELISA section). Brains were cryosectioned at a thickness of 20 µm and then fixed in 4% PFA as previously described. Sections were blocked with 5% normal donkey serum (Vector Laboratories)/0.1%Triton-X/0.01 M PBS for 1 h and incubated with primary antibodies diluted in blocking solution overnight at 4 °C. After incubation with primary antibodies, sections were washed in PBS and incubated with fluorophore-conjugated secondary antibodies (see below) and then mounted onto slides with fluorescence mounting medium (Dako). The following primary and secondary antibodies were used, respectively: for pericyte coverage, polyclonal goat anti-mouse aminopeptidase N/ANPEP (CD13) (R&D systems AF2335, 1:100 dilution) and Alexa Fluor 488- or 568-conjugated donkey anti-goat (Invitrogen, A-11055 or A-11057, 1:500 dilution); for fibrin/fibrinogen, polyclonal rabbit anti-human fibrinogen (Dako A0080, 1:500 dilution) and Alexa Fluor 488-conjugated donkey anti-rabbit (Invitrogen, A-21206,1:500 dilution); for tight junction proteins (zonula occludens), rabbit anti-mouse ZO-1 (Invitrogen 40–2200, 1:200 dilution) and Alexa Fluor 568-conjugated donkey anti-rabbit (Invitrogen A-10042, 1:500 dilution); and for occludin, mouse anti-mouse occludin (Invitrogen clone OC-3F10 no. 33-1500, 1:100 dilution) and Alexa Fluor 488-conjugated donkey anti-mouse (Invitrogen A-21202, 1:500 dilution); for CypA, rabbit anti-mouse CypA (Abcam ab42408, 1:100 dilution) and Alexa Fluor 488 or 568-conjugated donkey anti-rabbit (Invitrogen A-21206 or A-10042, 1:500 dilution); for MMP9, rabbit anti-mouse MMP9 (Abcam, ab38898, 1:100 dilution) and Alexa Fluor 488 or 568-conjugated donkey anti-rabbit (Invitrogen A-21206 or A-10042, 1:500 dilution); for amyloid-β, rabbit anti-human β-amyloid (Cell Signaling 8243S, 1:500 dilution) and Alexa Fluor 647-conjugated donkey anti-rabbit (Invitrogen A-31573,1:500 dilution); for neurofilament, mouse monoclonal anti-axonal neurofilament marker (SMI312) (BioLegend SMI312, 1:500 dilution) and Alexa Fluor 488-conjugated donkey anti-mouse (Invitrogen A-21202, 1:500 dilution); and for neuronal, polyclonal rabbit anti-NeuN (Millipore ABN78, 1:500 dilution) and Alexa Fluor 488 or 568-conjugated donkey anti-rabbit (Invitrogen, A-21206 or A-10042; 1:500 dilution). To visualize brain microvessels, sections were incubated with Dylight 488, 594 or 647-conjugated *Lycopersicon esculentum* lectin (Vector Labs, DL-1174; 1:200 dilution) for 1 h. Sections were imaged with a Zeiss LSM 510 confocal laser-scanning microscope or BZ9000 fluorescence microscope. Z-stack projections and pseudo-coloring were performed using ZEN software (Carl Zeiss Microimaging). Image post-analysis was performed using ImageJ software.

Microscopy analysis. For extravascular brain capillary leakages, pericyte coverage, tight junction protein analysis, CypA and MMP9 quantifications and NeuN$^+$ neuron counts and neurofilament (SMI312)$^+$ axons, 4–6 randomly selected fields in the somatosensory cortex region and/or the CA1 region of the hippocampus were analyzed for each animal in 3–4 nonadjacent sections (~100 µm apart) and averaged per mouse. For Aβ load, whole cortices and hippocampi were used, corresponding to the areas used for Aβ ELISA.

Extravascular leakages. For detection of extravascular brain capillary fibrinogen deposits, an antibody that detects both fibrinogen and fibrinogen-derived fibrin polymers was used. Ten-micron maximum projection z-stacks were reconstructed and the fibrinogen$^+$ perivascular signal on the abluminal side of lectin$^+$ endothelial profiles on microvessels ≤6 µm in diameter was analyzed using ImageJ software Integrated density analysis measurement tool, as we previously described[41].

Pericyte coverage. Ten-micron maximum projection z-stacks were reconstructed and the areas occupied by CD13$^+$ pericytes on lectin$^+$ endothelial profiles on microvessels ≤6 µm in diameter was analyzed using ImageJ as we previously described[65].

Immunofluorescent ZO-1 and occludin tight junction analysis. The length of ZO-1$^+$ and occludin$^+$ immunofluorescent signal on lectin$^+$ endothelial brain capillary profiles (<6 µm in diameter) in the cortex and the hippocampus was determined using the ImageJ Area measurement tool and expressed in mm of ZO-1 and occludin length per mm^2 of the total area of lectin$^+$ endothelial capillary profiles, as we previously described[6].

Microvascular length. Ten-micron maximum projection z-stacks were reconstructed and the length of lectin$^+$ endothelial capillary profiles (≤6 µm in diameter) was measured using the ImageJ plugin 'Neuro J' length analysis tool, as previously described[41,65]. The length was expressed in mm of lectin$^+$ endothelial capillary profiles per mm^3 of brain tissue.

Immunofluorescent CypA detection. The area occupied by CypA$^+$ immunofluorescent signal on CD13$^+$ pericytes was expressed as the percentage of CD13$^+$ pericyte area using the ImageJ Area measurement tool as we previously described[3]. Orthogonal views of confocal images of CypA, the pericyte marker CD13 and lectin$^+$ endothelium showing colocalization of CypA with CD13$^+$ pericytes were generated from a single-plane projection from a 20 single-plane z-stack using ZEN software (black edition). For the correlation analyses between CypA$^+$ pericytes and ZO-1 length and CypA$^+$ pericytes and occludin length

immunostaining for CypA and CD13, ZO-1 and lectin-endothelial staining and occludin and lectin-endothelial staining was performed on adjacent sections.

Immunofluorescent MMP9 detection. The area occupied by MMP9$^+$ immunofluorescent signal on CD13$^+$ pericytes was expressed as the percentage of CD13$^+$ pericyte area using the ImageJ Area measurement tool as we previously described[3]. Orthogonal views of confocal images of MMP9, the pericyte marker CD13 and lectin$^+$ endothelium showing colocalization of MMP9 with CD13$^+$ pericytes were generated from a single-plane projection from a 20 single-plane z-stack using ZEN software (black edition). For the correlation analyses between MMP9$^+$ pericytes and ZO-1 length and MMP9$^+$ pericytes and occludin length immunostaining for MMP9 and CD13, ZO-1 and lectin-endothelial staining and occludin and lectin-endothelial staining was performed on adjacent sections.

Aβ load. Primary somatosensory cortex and hippocampus were analyzed separately and the percentage area occupied by amyloid was quantified using Otsu-thresholding in ImageJ, as previously described[37].

NeuN$^+$ neuronal nuclei counting. NeuN$^+$ neurons were quantified using the ImageJ Cell Counter analysis tool, as previously described[6].

Neurofilament (SMI312)$^+$ axons. As we previously described[6,41], 10-µm maximum projection z-stacks were reconstructed and SMI312$^+$ signal was subjected to threshold processing and analysis using ImageJ.

Human Aβ40 and Aβ42 ELISA. Cortices and hippocampi were isolated and snap-frozen from one brain hemisphere (the other hemisphere was used for immunohistochemical assays; see Immunohistochemistry section). Cortices and hippocampi were sequentially extracted with sonication, first extracted with ten volumes of Tris-buffered saline with complete protease inhibitor cocktail (Roche), centrifuged at 20,000*g* for 30 min at 4 °C, followed by homogenization of pellet in ice-cold guanidine buffer (5 M guanidine hydrochloride/50 mM Tris HCl, pH 8). Guanidine extracts were diluted 1:200 and 1:20,000 for measurement of human Aβ40 and Aβ42, respectively by a Meso Scale Discovery assay (K15200E-1).

Statistical analysis. Sample sizes were calculated using nQUERY assuming a two-sided α-level of 0.05, 80% power and homogeneous variances for the samples to be compared, with the means and common s.d. for different parameters predicted from published data and our previous studies. For comparison between two groups, an *F* test was conducted to determine the similarity in the variances between the groups that are statistically compared and statistical significance was analyzed by unpaired two-tailed Student's *t*-test. Lilliefors test was used to test normality of the data (XLSTAT). For multiple comparisons, the *F* test was also used to determine the equality of variances between the groups compared and one-way ANOVA followed by Tukey's post hoc test, which was used to test statistical significance. For correlation analyses, we employed Pearson's correlation coefficient to measure the strength of the linear relationship between two variables. All analyses were performed using GraphPad Prism v.8.4.2 software and by an investigator blinded to the experimental conditions. Data are presented as violin plots with median and interquartile range as indicated in figure legends. A *P* value >0.05 was considered statistically not significant.

Reporting Summary. Further information on research design is available in the Nature Research Reporting Summary linked to this article.

Data availability

The data that support the findings of this study are available from the corresponding author upon request. We also provided a complete data source (Excel sheets for data panels of Figs. 1–8 and Extended Data Figs. 1–4) with corresponding statistical analysis.

Received: 28 October 2020; Accepted: 5 May 2021;
Published online: 14 June 2021

References

1. Yamazaki, Y., Zhao, N., Caulfield, T. R., Liu, C. C. & Bu, G. Apolipoprotein E and Alzheimer disease: pathobiology and targeting strategies. *Nat. Rev. Neurol.* **15**, 501–518 (2019).
2. Halliday, M. R. et al. Accelerated pericyte degeneration and blood–brain barrier breakdown in apolipoprotein E4 carriers with Alzheimer's disease. *J. Cereb. Blood Flow Metab.* **36**, 216–227 (2016).
3. Bell, R. D. et al. Apolipoprotein E controls cerebrovascular integrity via cyclophilin A. *Nature* **485**, 512–516 (2012).
4. Armulik, A. et al. Pericytes regulate the blood–brain barrier. *Nature* **468**, 557–561 (2010).
5. Bell, R. D. et al. Pericytes control key neurovascular functions and neuronal phenotype in the adult brain and during brain aging. *Neuron* **68**, 409–427 (2010).
6. Nikolakopoulou, A. M. et al. Pericyte loss leads to circulatory failure and pleiotrophin depletion causing neuron loss. *Nat. Neurosci.* **22**, 1089–1098 (2019).
7. Thambisetty, M., Beason-Held, L., An, Y., Kraut, M. A. & Resnick, S. M. APOE epsilon4 genotype and longitudinal changes in cerebral blood flow in normal aging. *Arch. Neurol.* **67**, 93–98 (2010).
8. Michels, L. et al. Arterial spin labeling imaging reveals widespread and Aβ-independent reductions in cerebral blood flow in elderly apolipoprotein epsilon-4 carriers. *J. Cereb. Blood Flow Metab.* **36**, 581–595 (2016).
9. Reiman, E. M. et al. Functional brain abnormalities in young adults at genetic risk for late-onset Alzheimer's dementia. *Proc. Natl Acad. Sci. USA* **101**, 284–289 (2004).
10. Koizumi, K. et al. Apoepsilon4 disrupts neurovascular regulation and undermines white matter integrity and cognitive function. *Nat. Commun.* **9**, 3816 (2018).
11. Mahley, R. W. & Huang, Y. Apolipoprotein E sets the stage: response to injury triggers neuropathology. *Neuron* **76**, 871–885 (2012).
12. Shi, Y. et al. ApoE4 markedly exacerbates tau-mediated neurodegeneration in a mouse model of tauopathy. *Nature* **549**, 523–527 (2017).
13. Deane, R. et al. apoE isoform-specific disruption of amyloid β peptide clearance from mouse brain. *J. Clin. Invest.* **118**, 4002–4013 (2008).
14. Huynh, T. V., Davis, A. A., Ulrich, J. D. & Holtzman, D. M. Apolipoprotein E and Alzheimer's disease: the influence of apolipoprotein E on amyloid-β and other amyloidogenic proteins. *J. Lipid Res.* **58**, 824–836 (2017).
15. Holtzman, D. M. et al. Apolipoprotein E isoform-dependent amyloid deposition and neuritic degeneration in a mouse model of Alzheimer's disease. *Proc. Natl Acad. Sci. USA* **97**, 2892–2897 (2000).
16. Hudry, E. et al. Gene transfer of human Apoe isoforms results in differential modulation of amyloid deposition and neurotoxicity in mouse brain. *Sci. Transl. Med.* **5**, 212ra161 (2013).
17. Montagne, A. et al. APOE4 leads to blood–brain barrier dysfunction predicting cognitive decline. *Nature* **581**, 71–76 (2020).
18. Wardlaw, J. M. et al. Neuroimaging standards for research into small vessel disease and its contribution to ageing and neurodegeneration. *Lancet Neurol* **12**, 822–838 (2013).
19. Kapasi, A., DeCarli, C. & Schneider, J. A. Impact of multiple pathologies on the threshold for clinically overt dementia. *Acta Neuropathol.* **134**, 171–186 (2017).
20. Iturria-Medina, Y. et al. Early role of vascular dysregulation on late-onset Alzheimer's disease based on multifactorial data-driven analysis. *Nat. Commun.* **7**, 11934 (2016).
21. Sweeney, M. D. et al. Vascular dysfunction: the disregarded partner of Alzheimer's disease. *Alzheimers Dement.* **15**, 158–167 (2019).
22. Iadecola, C. The neurovascular unit coming of age: a journey through neurovascular coupling in health and disease. *Neuron* **96**, 17–42 (2017).
23. Montagne, A. et al. Blood–brain barrier breakdown in the aging human hippocampus. *Neuron* **85**, 296–302 (2015).
24. van de Haar, H. J. et al. Neurovascular unit impairment in early Alzheimer's disease measured with magnetic resonance imaging. *Neurobiol. Aging* **45**, 190–196 (2016).
25. van de Haar, H. J. et al. Blood–Brain barrier leakage in patients with early Alzheimer disease. *Radiology* **281**, 527–535 (2016).
26. Nation, D. A. et al. Blood–brain barrier breakdown is an early biomarker of human cognitive dysfunction. *Nat. Med.* **25**, 270–276 (2019).
27. Jack, C. R. Jr. et al. NIA-AA research framework: toward a biological definition of Alzheimer's disease. *Alzheimers Dement.* **14**, 535–562 (2018).
28. Sullivan, P. M. et al. Targeted replacement of the mouse apolipoprotein E gene with the common human APOE3 allele enhances diet-induced hypercholesterolemia and atherosclerosis. *J. Biol. Chem.* **272**, 17972–17980 (1997).
29. Oakley, H. et al. Intraneuronal β-amyloid aggregates, neurodegeneration, and neuron loss in transgenic mice with five familial Alzheimer's disease mutations: potential factors in amyloid plaque formation. *J. Neurosci.* **26**, 10129–10140 (2006).
30. Youmans, K. L. et al. APOE4-specific changes in Aβ accumulation in a new transgenic mouse model of Alzheimer disease. *J. Biol. Chem.* **287**, 41774–41786 (2012).
31. Nishitsuji, K., Hosono, T., Nakamura, T., Bu, G. & Michikawa, M. Apolipoprotein E regulates the integrity of tight junctions in an isoform-dependent manner in an in vitro blood–brain barrier model. *J. Biol. Chem.* **286**, 17536–17542 (2011).
32. Alata, W., Ye, Y., St-Amour, I., Vandal, M. & Calon, F. Human apolipoprotein E varepsilon4 expression impairs cerebral vascularization and blood–brain barrier function in mice. *J. Cereb. Blood Flow Metab.* **35**, 86–94 (2015).
33. Cacciottolo, M. et al. The APOE4 allele shows opposite sex bias in microbleeds and Alzheimer's disease of humans and mice. *Neurobiol. Aging* **37**, 47–57 (2016).

34. Kook, S. Y. et al. Aβ(1)(-)(4)(2)-RAGE interaction disrupts tight junctions of the blood–brain barrier via Ca(2)(+)-calcineurin signaling. *J. Neurosci.* **32**, 8845–8854 (2012).
35. Giannoni, P. et al. Cerebrovascular pathology during the progression of experimental Alzheimer's disease. *Neurobiol. Dis.* **88**, 107–117 (2016).
36. Park, J. C. et al. Annexin A1 restores Aβ1-42 -induced blood–brain barrier disruption through the inhibition of RhoA-ROCK signaling pathway. *Aging Cell* **16**, 149–161 (2017).
37. Lazic, D. et al. 3K3A-activated protein C blocks amyloidogenic BACE1 pathway and improves functional outcome in mice. *J. Exp. Med.* **216**, 279–293 (2019).
38. Eguchi, K. et al. Whole-brain low-intensity pulsed ultrasound therapy markedly improves cognitive dysfunctions in mouse models of dementia: crucial roles of endothelial nitric oxide synthase. *Brain Stimul.* **11**, 959–973 (2018).
39. Neuman, K. M. et al. Evidence for Alzheimer's disease-linked synapse loss and compensation in mouse and human hippocampal CA1 pyramidal neurons. *Brain Struct. Funct.* **220**, 3143–3165 (2015).
40. Balu, D. et al. The role of APOE in transgenic mouse models of AD. *Neurosci. Lett.* **707**, 134285 (2019).
41. Montagne, A. et al. Pericyte degeneration causes white matter dysfunction in the mouse central nervous system. *Nat. Med.* **24**, 326–337 (2018).
42. Thomas, R. et al. Epidermal growth factor prevents APOE4 and amyloid-β-induced cognitive and cerebrovascular deficits in female mice. *Acta Neuropathol. Commun.* **4**, 111 (2016).
43. Sagare, A. P. et al. Pericyte loss influences Alzheimer-like neurodegeneration in mice. *Nat. Commun.* **4**, 2932 (2013).
44. Park, L. et al. Innate immunity receptor CD36 promotes cerebral amyloid angiopathy. *Proc. Natl Acad. Sci. USA* **110**, 3089–3094 (2013).
45. Park, L. et al. Age-dependent neurovascular dysfunction and damage in a mouse model of cerebral amyloid angiopathy. *Stroke* **45**, 1815–1821 (2014).
46. Stanciu, C., Trifan, A., Muzica, C. & Sfarti, C. Efficacy and safety of alisporivir for the treatment of hepatitis C infection. *Expert Opin. Pharmacother.* **20**, 379–384 (2019).
47. Softic, L. et al. Inhibition of SARS-CoV-2 infection by the cyclophilin inhibitor alisporivir (Debio 025). *Antimicrob. Agents Chemother.* **64**, e00876–20 (2020).
48. Millay, D. P. et al. Genetic and pharmacologic inhibition of mitochondrial-dependent necrosis attenuates muscular dystrophy. *Nat. Med.* **14**, 442–447 (2008).
49. Tiepolo, T. et al. The cyclophilin inhibitor Debio 025 normalizes mitochondrial function, muscle apoptosis and ultrastructural defects in Col6a1$^{-/-}$ myopathic mice. *Br. J. Pharmacol.* **157**, 1045–1052 (2009).
50. Nikolakopoulou, A. M. et al. Endothelial LRP1 protects against neurodegeneration by blocking cyclophilin A. *J. Exp. Med.* **218**, e20202207 (2021).
51. Tai, L. M. et al. EFAD transgenic mice as a human APOE relevant preclinical model of Alzheimer's disease. *J. Lipid Res.* **58**, 1733–1755 (2017).
52. Eimer, W. A. & Vassar, R. Neuron loss in the 5XFAD mouse model of Alzheimer's disease correlates with intraneuronal Aβ42 accumulation and caspase-3 activation. *Mol. Neurodegener.* **8**, 2 (2013).
53. Senatorov, V. V. Jr. et al. Blood–brain barrier dysfunction in aging induces hyperactivation of TGFβ signaling and chronic yet reversible neural dysfunction. *Sci. Transl. Med.* **11**, eaaw8283 (2019).
54. Andreone, B. J. et al. Blood–brain barrier permeability is regulated by lipid transport-dependent suppression of caveolae-mediated transcytosis. *Neuron* **94**, 581–594 (2017).
55. Deane, R. et al. LRP/amyloid β-peptide interaction mediates differential brain efflux of Aβ isoforms. *Neuron* **43**, 333–344 (2004).
56. Shibata, M. et al. Clearance of Alzheimer's amyloid-ss(1-40) peptide from brain by LDL receptor-related protein-1 at the blood–brain barrier. *J. Clin. Invest.* **106**, 1489–1499 (2000).
57. Donahue, J. E. et al. RAGE, LRP-1, and amyloid-β protein in Alzheimer's disease. *Acta Neuropathol.* **112**, 405–415 (2006).
58. Zhao, Z. et al. Central role for PICALM in amyloid-β blood–brain barrier transcytosis and clearance. *Nat. Neurosci.* **18**, 978–987 (2015).
59. Winkler, E. A. et al. GLUT1 reductions exacerbate Alzheimer's disease vasculo-neuronal dysfunction and degeneration. *Nat. Neurosci.* **18**, 521–530 (2015).
60. Jaeger, L. B. et al. Testing the neurovascular hypothesis of Alzheimer's disease: LRP-1 antisense reduces blood–brain barrier clearance, increases brain levels of amyloid-β protein, and impairs cognition. *J. Alzheimers Dis.* **17**, 553–570 (2009).
61. Barnes, S. R. et al. ROCKETSHIP: a flexible and modular software tool for the planning, processing and analysis of dynamic MRI studies. *BMC Med. Imaging* **15**, 19 (2015).
62. Barnes, S. R. et al. Optimal acquisition and modeling parameters for accurate assessment of low Ktrans blood–brain barrier permeability using dynamic contrast-enhanced MRI. *Magn. Reson. Med.* **75**, 1967–1977 (2016).
63. Ostergaard, L., Weisskoff, R. M., Chesler, D. A., Gyldensted, C. & Rosen, B. R. High resolution measurement of cerebral blood flow using intravascular tracer bolus passages. Part I: mathematical approach and statistical analysis. *Magn. Reson. Med.* **36**, 715–725 (1996).
64. Wu, O. et al. Tracer arrival timing-insensitive technique for estimating flow in MR perfusion-weighted imaging using singular value decomposition with a block-circulant deconvolution matrix. *Magn. Reson. Med.* **50**, 164–174 (2003).
65. Nikolakopoulou, A. M., Zhao, Z., Montagne, A. & Zlokovic, B. V. Regional early and progressive loss of brain pericytes but not vascular smooth muscle cells in adult mice with disrupted platelet-derived growth factor receptor-β signaling. *PLoS ONE* **12**, e0176225 (2017).

Acknowledgements

The work of B.V.Z. is supported by the National Institutes of Health grant nos. R01NS034467, R01AG023084, R01AG039452 and 1R01NS100459, in addition to Cure Alzheimer's Fund and the Foundation Leducq Transatlantic Network of Excellence for the Study of Perivascular Spaces in Small Vessel Disease reference no. 16 CVD 05. We thank V. Li for technical assistance with some experiments.

Author contributions

A.M., A.M.N., M.T.H., A.P.S. and B.V.Z. designed the research study and analyzed and interpreted the data. A.M. and M.T.H. performed MRI scans and MRI data analyses. M.S. helped with MRI data analyses. A.M.N., M.T.H. and A.P.S. performed brain tissue assays. A.P.S. performed amyloid assays. E.J.L., D.L. and S.V.R. performed behavioral tests. E.Z., A.G. and C.-J.H. performed tissue collection. A.M., S.R.B. and J.P. developed our in-house DSC-MRI program. M.J.L. provided human *APOE* mice crossed with *5xFAD* line. M.J.L. and R.E.J. provided critical reading of the manuscript. A.M. contributed to manuscript writing and B.V.Z. supervised all data analysis and interpretation and wrote the manuscript.

Competing interests

The authors declare no competing interests.

Additional information

Extended data is available for this paper at https://doi.org/10.1038/s43587-021-00073-z.

Supplementary information The online version contains supplementary material available at https://doi.org/10.1038/s43587-021-00073-z.

Correspondence and requests for materials should be addressed to B.V.Z.

Peer review information *Nature Aging* thanks Jan Klohs, and the other, anonymous reviewer(s) for their contribution to the peer review of this work.

Reprints and permissions information is available at www.nature.com/reprints.

Publisher's note Springer Nature remains neutral with regard to jurisdictional claims in published maps and institutional affiliations.

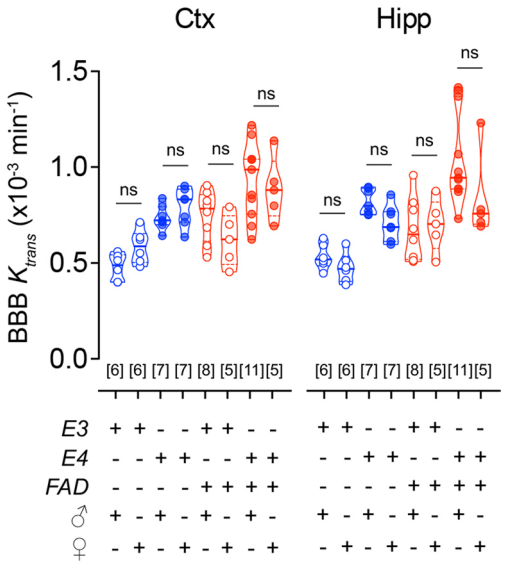

Extended Data Fig. 1 | Additional characterization of blood-brain barrier breakdown in old *APOE4* and *APOE4;5xFAD* male and female mice. Blood-brain barrier (BBB) permeability K_{trans} values in the cortex (Ctx) and hippocampus (Hipp) in male and female *E3* (n = 12, 6 ♂ and 6 ♀; blue empty circles), *E4* (n = 14, 7 ♂ and 7 ♀; blue filled circles), *E3+FAD* (n = 13, 8 ♂ and 5 ♀; red empty circles), and *E4+FAD* (n = 16, 11 ♂ and 5 ♀; red filled circles) mice generated from dynamic contrast-enhanced magnetic resonance scans. Mice (both genders) were 18–24-month old. Data are presented as truncated violin plots; continuous line, median; dotted line, interquartile range. Significance by one-way ANOVA followed by the Tukey post hoc test; ns, non-significant.

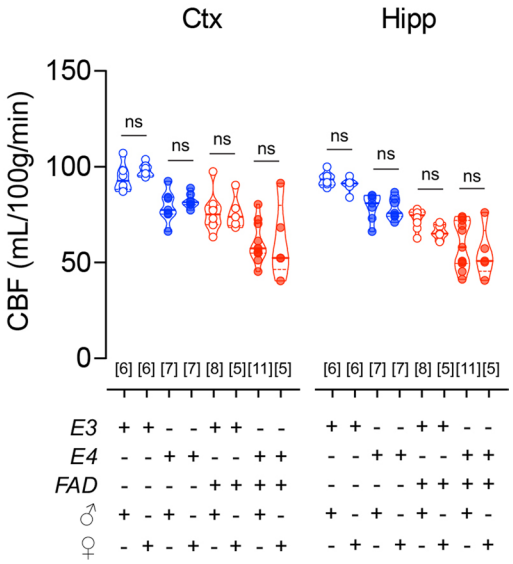

Extended Data Fig. 2 | Additional characterization of cerebral blood flow reductions in old *APOE4* and *APOE4;5xFAD* male and female mice. Cerebral blood flow (CBF) values in the cortex (Ctx) and hippocampus (Hipp) in male and female *E3* (n = 12, 6 ♂ and 6 ♀; blue empty circles), *E4* (n = 14, 7 ♂ and 7 ♀; blue filled circles), *E3+FAD* (n = 13, 8 ♂ and 5 ♀; red empty circles), and *E4+FAD* (n = 16, 11 ♂ and 5 ♀; red filled circles) mice generated from dynamic susceptibility-contrast magnetic resonance scans. Mice (both genders) were 18–24-month old. Data are presented as truncated violin plots; continuous line, median; dotted line, interquartile range. Significance by one-way ANOVA followed by the Tukey post hoc test; ns, non-significant.

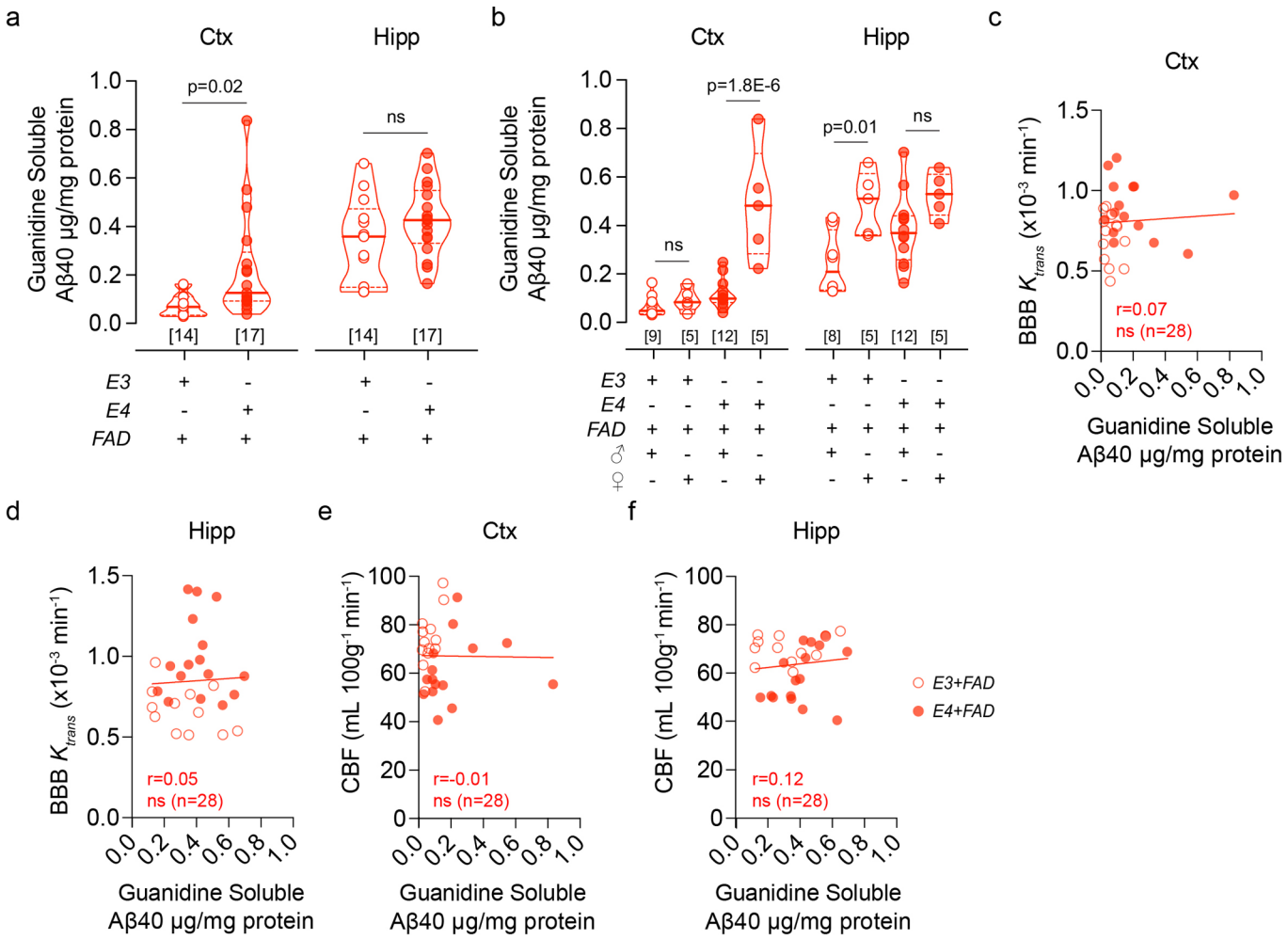

Extended Data Fig. 3 | Additional characterization of Aβ pathology in old *APOE3;5xFAD* and *APOE4;5xFAD* male and female mice and Aβ-independent vascular changes. a Aβ40 levels in the Ctx and Hipp in *E3+FAD* (n=14) and *E4+FAD* (n=17) mice. **b**, Aβ40 levels in the Ctx and Hipp in male and female *E3+FAD* (n=13-14, 8-9 ♂ and 5 ♀) and *E4+FAD* (n=17, 12 ♂ and 5 ♀) mice. Data are presented as truncated violin plots; continuous line, median; dotted line, interquartile range. **c-f**, Lack of correlation between the blood-brain barrier (BBB) permeability K_{trans} values and Aβ40 levels in the Ctx and Hipp (**c,d**) and regional cerebral blood flow (CBF) values and Aβ40 levels in the Ctx and Hipp (**e,f**). Mice (both genders) were 18-24-month old (n=28 individual points from both groups). In **a**, significance by unpaired two-tailed Student *t*-tests. In **b**, significance by one-way ANOVA followed by the Tukey post hoc test. In **c-f**, significance by two-tailed simple linear regression; r, Pearson correlation; ns, non-significant.

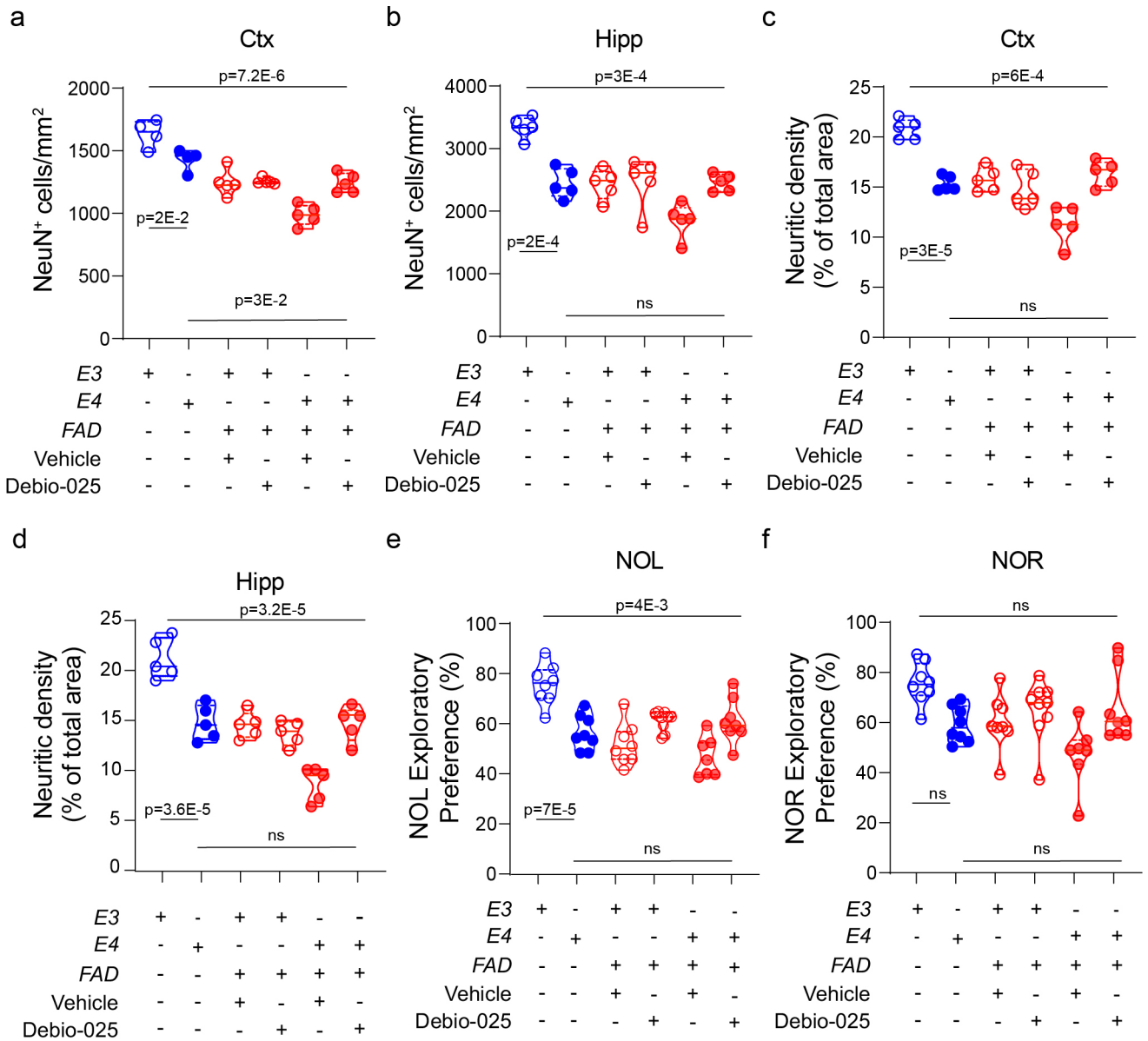

Extended Data Fig. 4 | Effects of Debio-025 relative to vehicle on neuron counts, neuritic density and behavior in *APOE4;5xFAD* and *APOE3;5xFAD* mice (red circles, data taken from Fig. 8) compared to the littermate controls without *5XFAD* transgenes (blue circles). a–d, Quantification of NeuN+-neurons (**a,b**) and SMI312+-neuritic density (**c,d**) in the Ctx and Hipp in *E3* (blue empty circles) and *E4* (blue filled circles) untreated littermate controls without *5xFAD* transgenes compared to age-matched *E3+FAD* (red empty circles) and *E4+FAD* (red filled circles) mice treated with vehicle or Debio-025; In **a-d**, n = 5 mice per group except in **a**. n = 4 in for *E3* littermate controls without *5XFAD* transgenes. **e,f**, Novel object location (NOL; **e**) and novel object recognition (NOR; **f**) in *E3* (n = 8, blue empty circles) and *E4* (n = 8, blue filled circles) untreated littermate controls without *5XFAD* transgenes compared to age-matched *E3+FAD* vehicle-treated (n = 8; red empty circles), *E3+FAD* Debio-025-treated (n = 9; red empty circles), *E4+FAD* vehicle-treated (n = 7; red filled circles), and *E4+FAD* Debio-025-treated (n = 8; red filled circles) mice. Mice (both genders) were 10–12-month-old. In all graphs, data for *E3+FAD* and *E4+FAD* animals are the same as in Fig. 8 (red circles empty and filled); new data used for comparison are from their respective untreated littermate controls without *5XFAD* transgenes (blue circles empty and filled). All data are presented as violin plots; continuous line, median; dotted line, interquartile range. Significance by one-way ANOVA followed by the Tukey post hoc test.

nature research

Corresponding author(s): Berislav V Zlokovic

Last updated by author(s): 4/22/2021

Reporting Summary

Nature Research wishes to improve the reproducibility of the work that we publish. This form provides structure for consistency and transparency in reporting. For further information on Nature Research policies, see our Editorial Policies and the Editorial Policy Checklist.

Statistics

For all statistical analyses, confirm that the following items are present in the figure legend, table legend, main text, or Methods section.

n/a	Confirmed	
☐	☒	The exact sample size (*n*) for each experimental group/condition, given as a discrete number and unit of measurement
☐	☒	A statement on whether measurements were taken from distinct samples or whether the same sample was measured repeatedly
☐	☒	The statistical test(s) used AND whether they are one- or two-sided *Only common tests should be described solely by name; describe more complex techniques in the Methods section.*
☐	☒	A description of all covariates tested
☐	☒	A description of any assumptions or corrections, such as tests of normality and adjustment for multiple comparisons
☐	☒	A full description of the statistical parameters including central tendency (e.g. means) or other basic estimates (e.g. regression coefficient) AND variation (e.g. standard deviation) or associated estimates of uncertainty (e.g. confidence intervals)
☐	☒	For null hypothesis testing, the test statistic (e.g. *F*, *t*, *r*) with confidence intervals, effect sizes, degrees of freedom and *P* value noted *Give P values as exact values whenever suitable.*
☒	☐	For Bayesian analysis, information on the choice of priors and Markov chain Monte Carlo settings
☒	☐	For hierarchical and complex designs, identification of the appropriate level for tests and full reporting of outcomes
☐	☒	Estimates of effect sizes (e.g. Cohen's *d*, Pearson's *r*), indicating how they were calculated

Our web collection on statistics for biologists contains articles on many of the points above.

Software and code

Policy information about availability of computer code

Data collection	All MRI scans were acquired using Preclinical Scan software version 4.0.2.10
Data analysis	In-house T1 mapping/DCE processing software (Rocketship) implemented in Matlab, available here: https://github.com/petmri/ROCKETSHIP. ImageJ 1.48v was used for MRI and histology image processing. GraphPad Prism 8.4.2 was used to analyze the data. nQuery Advanced 8.5.2 software was used to estimate sample sizes.

For manuscripts utilizing custom algorithms or software that are central to the research but not yet described in published literature, software must be made available to editors and reviewers. We strongly encourage code deposition in a community repository (e.g. GitHub). See the Nature Research guidelines for submitting code & software for further information.

Data

Policy information about availability of data

All manuscripts must include a data availability statement. This statement should provide the following information, where applicable:

- Accession codes, unique identifiers, or web links for publicly available datasets
- A list of figures that have associated raw data
- A description of any restrictions on data availability

The data that support the findings of this study are available from the corresponding author upon request. We also provided a complete data source – excel sheets for all main Figures 1-8 data panels and the Extended Data Figures 1-4 data panels with the corresponding statistical analysis.

Field-specific reporting

Please select the one below that is the best fit for your research. If you are not sure, read the appropriate sections before making your selection.

☒ Life sciences ☐ Behavioural & social sciences ☐ Ecological, evolutionary & environmental sciences

For a reference copy of the document with all sections, see nature.com/documents/nr-reporting-summary-flat.pdf

Life sciences study design

All studies must disclose on these points even when the disclosure is negative.

Sample size	Sample sizes were calculated using nQUERY assuming a two-sided alpha-level of 0.05, 80% power, and homogeneous variances for the samples to be compared, with the means and common standard deviation for different parameters predicted from published data and our previous studies.
Data exclusions	All animals were included in the study.
Replication	For each experiment, at least 5 animals were used. For each series of experiments, all replication attempts were successful.
Randomization	All animals were randomized for their genotype information.
Blinding	All experiments were blinded: the operators responsible for the experimental procedures and data analysis were blinded and unaware of group allocation throughout the experiments.

Reporting for specific materials, systems and methods

We require information from authors about some types of materials, experimental systems and methods used in many studies. Here, indicate whether each material, system or method listed is relevant to your study. If you are not sure if a list item applies to your research, read the appropriate section before selecting a response.

Materials & experimental systems

n/a	Involved in the study
☐	☒ Antibodies
☒	☐ Eukaryotic cell lines
☒	☐ Palaeontology and archaeology
☐	☒ Animals and other organisms
☒	☐ Human research participants
☒	☐ Clinical data
☒	☐ Dual use research of concern

Methods

n/a	Involved in the study
☒	☐ ChIP-seq
☒	☐ Flow cytometry
☐	☒ MRI-based neuroimaging

Antibodies

Antibodies used	All antibodies are listed in the method section. The following primary and secondary antibodies were used, respectively: for pericyte coverage, polyclonal goat anti-mouse aminopeptidase N/ANPEP (CD13) (R&D systems AF2335, 1:100) and Alexa fluor 488- or 568-conjugated donkey anti-goat (Invitrogen, A-11055 or A-11057, 1:500); for fibrin/fibrinogen, polyclonal rabbit anti-human fibrinogen (Dako A0080, 1:500) and Alexa fluor 488-conjugated donkey anti-rabbit (Invitrogen, A-21206,1:500); for tight junction proteins - zonula occludens, rabbit anti-mouse ZO-1 (Invitrogen 40-2200, 1:200) and Alexa fluor 568-conjugated donkey anti-rabbit (Invitrogen A-10042, 1:500), and for occludin, mouse anti-mouse occludin (Invitrogen clone OC-3F10 #33-1500, 1:100) and Alexa fluor 488-conjugated donkey anti-mouse (Invitrogen A-21202, 1:500); for CypA, rabbit anti-mouse CypA (Abcam ab42408, 1:100) and Alexa fluor 488 or 568- -conjugated donkey anti-rabbit (Invitrogen A-21206 or A-10042, 1:500); for MMP9, rabbit anti-mouse MMP9 (Abcam, ab38898, 1:100) and Alexa fluor 488 or 568-conjugated donkey anti-rabbit (Invitrogen A-21206 or A-10042, 1:500); for amyloid-β, rabbit anti-human β-amyloid (Cell Signaling 8243S, 1:500) and Alexa fluor 647-conjugated donkey anti-rabbit (Invitrogen A-31573,1:500); for neurofilament, mouse monoclonal anti-axonal neurofilament marker (SMI-312) (BioLegend SMI312, 1:500) and Alexa fluor 488-conjugated donkey anti-mouse (Invitrogen A-21202, 1:500), for neuronal, polyclonal rabbit anti-NeuN (Millipore ABN78, 1:500) and Alexa fluor 488 or 568- -conjugated donkey anti-rabbit (Invitrogen, A-21206 or A-10042; 1:500). To visualize brain microvessels, sections were incubated with Dylight 488, 594, or 647-conjugated L. esculentum lectin (Vector Labs, DL-1174; 1:200)
Validation	Antibodies were previously used by our lab and others, and data were published in literature and on manufacturer's websites: Primary Antibodies: Polyclonal goat anti-mouse aminopeptidase N/ANPEP (CD13; R&D systems, AF2335; 1:100): Montagne et al, Nat Med. 2018 Mar;24(3):326-337, Nikolakopoulou et al., Nat Neurosci. 2019 Jul;22(7):1089-1098 Polyclonal rabbit anti-human fibrinogen (Dako, A0080; 1:500): Montagne et al, Nat Med. 2018 Mar;24(3):326-337, and

Nikolakopoulou et al., Nat Neurosci. 2019 Jul;22(7):1089-1098
Polyclonal rabbit anti-mouse ZO-1 (Invitrogen, 40-2200; 1:200): Guo et al., Nat Med. 2018 May;24(4):438-449, and Nikolakopoulou et al., J. Exp. Med. 2021, 218 (4): e20202207.
Monoclonal mouse anti-mouse occludin (Invitrogen, clone OC-3F10, #33-1500, 1:100): Nikolakopoulou et al., Nat Neurosci. 2019 Jul;22(7):1089-1098 and Nikolakopoulou et al., J. Exp. Med. 2021, 218 (4): e20202207.
Polyclonal rabbit anti-human CypA (cross reacts with mouse CypA, Abcam, ab42408, 1:200): Bell et al., Nature. 2012 May 16;485(7399):512-6
Polyclonal rabbit anti-mouse MMP-9 (Abcam, ab38898; 1:200): Bell et al., Nature. 2012 May 16;485(7399):512-6
Polyclonal rabbit anti-human β-amyloid (Cell Signaling, 8243S, 1:500): Sagare et al., Nat Commun. 2013 Dec; 4:2932. doi: 10.1038/ncomms3932
Monoclonal mouse anti-mouse SMI-312 (BioLegend, SMI312; 1:500): Montagne et al, Nat Med. 2018 Mar;24(3):326-337, and Nikolakopoulou et al., Nat Neurosci. 2019 Jul;22(7):1089-1098
Polyclonal rabbit anti-mouse NeuN (Millipore, ABN78; 1:500): Montagne et al, Nat Med. 2018 Mar;24(3):326-337, and Nikolakopoulou et al., Nat Neurosci. 2019 Jul;22(7):1089-1098

Secondary Antibodies
Alexa fluor 488- or 568-conjugated donkey anti-goat (Invitrogen, A-11055 or A-11057; 1:500): Montagne et al, Nat Med. 2018 Mar;24(3):326-337 , and Nikolakopoulou et al., Nat Neurosci. 2019 Jul;22(7):1089-1098
Alexa fluor 488- or 568-conjugated donkey anti-mouse (Invitrogen, A-21202, A-10037; 1:500): Montagne et al, Nat Med. 2018 Mar;24(3):326-337, and Nikolakopoulou et al., Nat Neurosci. 2019 Jul;22(7):1089-1098
Alexa fluor 488, 568 or 647-conjugated donkey anti-rabbit (Invitrogen, A-21206, A-10042 or A-31573; 1:500): Montagne et al, Nat Med. 2018 Mar;24(3):326-337 and Nikolakopoulou et al., Nat Neurosci. 2019 Jul;22(7):1089-1098
Alexa fluor 647-conjugated goat anti-rabbit (Invitrogen, A-21247; 1:500): Montagne et al, Nat Med. 2018 Mar;24(3):326-337, and Nikolakopoulou et al., Nat Neurosci. 2019 Jul;22(7):1089-1098

Animals and other organisms

Policy information about studies involving animals; ARRIVE guidelines recommended for reporting animal research

Laboratory animals	Mice were housed in plastic cages on a 12 h light/dark cycle with ad libitum access to water and a standard laboratory diet. Room ambient temperature was set between 68-79 degrees Fahrenheit (20-26 degrees Celsius) and humidity was kept between 30-70%. Animals of both sexes at 18-24 months of age were used in the experiments. All animals were included in the study. All animals were randomized for their genotype information. All experiments were blinded; the operators responsible for the experimental procedures and data analysis were blinded and unaware of group allocation throughout the experiments. APOE3;5xFAD and APOE4;5xFAD mice - also commonly called E3FAD and E4FAD mice, respectively - were generated by crossing heterozygous 5xFAD+/- line (Tg6799 on a C57BL/6 and SJL background) that co-express five FAD mutations (APP K670N/M671L, I716V, V717I and PS1 M146L, L286V) under the control of the neuron-specific mouse Thy-1 promoter34 with homozygous human APOE3+/+ and APOE4+/+ targeted replacement mice33. APOE3;5xFAD and APOE4;5xFAD littermate controls or non-carriers derived from these litters were 5xFAD-/-;APOE3+/+ and 5xFAD-/-;APOE4+/+, respectively, that we refer to as APOE3 and APOE4 knock-in control mice. Breeding pairs were generously provided by Mary J LaDu (University of Illinois at Chicago). All animals were genotyped by PCR using protocols and primer sequences as described by the distributor or donating investigator. Males and females from both lines were used for breeding and to maintain the colony.
Wild animals	This study did not involve wild animals.
Field-collected samples	This study did not involve samples collected from the field.
Ethics oversight	All procedures were approved by the Institutional Animal Care and Use Committee at the University of Southern California with National Institutes of Health guidelines

Note that full information on the approval of the study protocol must also be provided in the manuscript.

Magnetic resonance imaging

Experimental design

Design type	The mice were scanned with either a Biospec 7T system (300 MHz, Bruker, Billerica, MA, USA) at the California Institute of Technology (Pasadena, CA, USA) or a MR Solutions 7T PET-MR system (MR Solutions Ltd., Guildford, UK) at the Zilkha Neurogenetic Institute (University of Southern California, Los Angeles, CA, USA). The Bruker system was equipped with the standard B-GA12 gradient set (~114-mm inner diameter; 400 mT.m-1 maximum gradient) and a 35-mm internal diameter quadrature volume coil (M2M Imaging, Cleveland, OH). The MR Solutions system was equipped with the MRS cryogen-free MRI system (bore size ~24-mm, up to 600 mT.m-1 maximum gradient) and a 20-mm internal diameter quadrature bird cage mouse head coil.
Design specifications	Total imaging time was approximately 40 min per mouse.
Behavioral performance measures	Mice were anesthetized by 1-1.5% isoflurane/air. Respiration rate (80 ± 10 breaths per minute) and body temperature (36.5 ± 0.5°C) are monitored during the experiments using an abdominal pressure-sensitive probe and a rectal temperature probe. The isoflurane dose and heated air flow was adjusted continuously to ensure stable and reproducible depth of anesthesia.

Acquisition

Imaging type(s): Dynamic contrast-enhanced (DCE)

Field strength: 7T

Sequence & imaging parameters: The sequences were collected in the following order: T2-weighted (2D-fast spin echo (FSE), TR/TE 4,900/45 ms, 34 slices, slice thickness 500 µm, in-plane resolution 70x70 µm2) to obtain structural images; dynamic contrast-enhanced (DCE) protocol for the blood-brain barrier permeability assessment; and finally, dynamic susceptibility-contrast (DSC) imaging for cerebral blood flow.
The DCE-MRI imaging protocol was performed within the dorsal hippocampus territory, and included measurement of pre-contrast T1-values using a variable flip angle (VFA) fast low angle shot (FLASH) sequence (FA = 5, 10, 15, 30 and 45°, TR/TE = 18 ms/4 ms, slice thickness 1 mm, in-plane resolution 85x85 µm2), followed by a dynamic series of 325 T1-weighted images with identical geometry and a temporal resolution of 4.6 s (FLASH, TR/TE 18 ms/4 ms, flip angle 15°, slice thickness 1 mm, in-plane resolution 85x85 µm2). Using a power injector, a bolus dose (140 µL) of 0.5 mmol/kg Gd-DTPA (Gadolinium-diethylenetriamine pentaacetic acid, BioPAL, Inc., diluted in saline 1:6) was injected via the tail vein at a rate of 600 µL/min. DCE images were collected for 5 min before and 20 min after the injection. The DSC-MRI imaging was performed on the exact same geometry. A dynamic series of 100 T2*-weighted images is used, with a temporal resolution of 1.5 s (FLASH, TR/TE 18 ms/4 ms, slice thickness 1 mm, flip angle 15°, in-plane resolution 170x270 µm2). A second bolus dose (140 µL) of Gd-DTPA (1:1) was injected via the tail vein at a rate of 1,000 µL/min. DSC images were collected over 120 s after the injection.

Area of acquisition: DCE scans: One coronal slice (thickness 1-mm) was selected within the dorsal hippocampus territory and the prefrontal cortex to guarantee having the hippocampus and primary somatosensory cortex as well as common carotid arteries for arterial input functions.

Diffusion MRI ☐ Used ☒ Not used

Preprocessing

Preprocessing software: To process in vivo T1-VFA and DCE scans, we used our in-house T1 mapping/DCE processing software (Rocketship) implemented in Matlab (Barnes, S. R. et al. ROCKETSHIP: a flexible and modular software tool for the planning, processing and analysis of dynamic MRI studies. BMC Med. Imaging 15, 19 (2015)). Available here: https://github.com/petmri/ROCKETSHIP.

Normalization: N/A, normalization to a template is not used for DCE or DSC MRI analyses. Imaging slices are selected individually to get the best possible arterial input function (AIF) for each animal.Ð1-mapping was performed for each individual animal before DCE-MRI to measure T1 relaxivity values.

Normalization template: N/A, see above

Noise and artifact removal: Motion correction was applied using ImageJ's Stack Reg - Rigid Body plugin when necessary.

Volume censoring: N/A, motion correction with Rigid Body plugin was sufficient to correct for motion that happened in rare cases. Anesthetized mice were secured in ear and bite bars for the imaging and motion during the MRI was minimal.

Statistical modeling & inference

Model type and settings: N/A

Effect(s) tested: We measured BBB permeability using DCE technique.

Specify type of analysis: ☐ Whole brain ☒ ROI-based ☐ Both

Anatomical location(s): ROIs for primary somatosensory cortex and dorsal hippocampus were manually assigned by an investigator blinded to groups using ImageJ. To examine distinct changes, regional ROIs were drawn on Ktrans using boundaries defined by the Allen brain atlas (http://mouse.brain-map.org/).

Statistic type for inference (See Eklund et al. 2016): Software packages or functional MRI measurements mentioned in Eklund et al. 2016 have not been used in this study.

Correction: N/A

Models & analysis

n/a	Involved in the study
☒	☐ Functional and/or effective connectivity
☒	☐ Graph analysis
☒	☐ Multivariate modeling or predictive analysis